THE ULTRA-LOW-ENERGY ISOTOPE SPECTROMETER (ULEIS) FOR THE ACE SPACECRAFT

G. M. MASON[1,2], R. E. GOLD[3], S. M. KRIMIGIS[3], J. E. MAZUR[1,*], G. B. ANDREWS[3], K. A. DALEY[1], J. R. DWYER[1], K. F. HEUERMAN[1], T. L. JAMES[1], M. J. KENNEDY[3], T. LEFEVERE[3], H. MALCOLM[3], B. TOSSMAN[3] and P. H. WALPOLE[1]

[1]*Department of Physics, University of Maryland, College Park, MD 20742, U.S.A.*
[2]*Institute for Physical Science and Technology, University of Maryland, U.S.A.*
[3]*Johns Hopkins University/Applied Physics Laboratory, Laurel, MD 20723, U.S.A.*

Abstract. The Ultra Low Energy Isotope Spectrometer (ULEIS) on the ACE spacecraft is an ultra high resolution mass spectrometer designed to measure particle composition and energy spectra of elements He–Ni with energies from ∼45 keV nucl^{-1} to a few MeV nucl^{-1}. ULEIS will investigate particles accelerated in solar energetic particle events, interplanetary shocks, and at the solar wind termination shock. By determining energy spectra, mass composition, and their temporal variations in conjunction with other ACE instruments, ULEIS will greatly improve our knowledge of solar abundances, as well as other reservoirs such as the local interstellar medium. ULEIS is designed to combine the high sensitivity required to measure low particle fluxes, along with the capability to operate in the largest solar particle or interplanetary shock events. In addition to detailed information for individual ions, ULEIS features a wide range of count rates for different ions and energies that will allow accurate determination of particle fluxes and anisotropies over short (∼few minutes) time scales.

1. Scientific Goals

The origin and evolution of the solar system and galaxy can be studied by measuring the composition of their condensed and gaseous materials. These compositional data contain information on processes that created the material in the big bang, in later nucleosynthetic processing, and, more recently, in fractionation processes associated with the condensation of the material from the interstellar medium into stars, planets, and smaller objects. Since astrophysical objects routinely accelerate ions to high energies, multiple streams of particles from a wide variety of sites fill the interplanetary space near Earth. These particle streams may be sampled, studied, and probed for information about their parent sites and the processes that accelerated and brought them here.

In the pioneering studies at the start of the space program, energetic particles detected in the interplanetary medium near Earth were thought to have two primary sources: the sun and galaxy. Solar energetic particles were energized in association

* Now at Aerospace Corp., Los Angeles, CA 90009, U.S.A.

Space Science Reviews **86:** 409–448, 1998.

with explosions (flares) visible on the solar surface. Galactic cosmic rays arrived from outside the solar system from an unknown source of such power that only processes involving supernovae seemed likely. Later, an additional particle source was identified wherein neutral atoms from the local interstellar gas had a single electron removed by (UV) sunlight, and then were energized by a shock in the outer solar system. Most recently, evidence has mounted for acceleration of ions from a new particle source: interstellar and interplanetary dust grains.

These samples of matter contain a rich lode of information about their parent sites, about astrophysical plasma processes that accelerate ions, and the conditions under which they can be transported over enormous distances to be found near Earth. Studies carried out to date have revealed that while each of these material samples contains a grossly similar composition, variations routinely occur, and these contain important new clues about the particle sites and the processes taking place there. For example, material flowing out of the sun (the solar wind) in the equatorial regions often shows enhancements of materials such as Iron and Magnesium compared to the abundances in the solar photosphere. Another case is the accelerated interstellar neutral material, which is rich in Nitrogen and Oxygen, and has very little Carbon in contrast to other sources in nature.

Recent advances in knowledge of the solar wind composition, and the composition of galactic cosmic rays, have highlighted the need for advanced instrumentation with the ability to detect differences between the various matter samples and other material reservoirs. For example, compared to meteoritic abundances the isotope ^{22}Ne had been found to be enriched in some samples of solar material, and not in others. The solar wind elemental composition over the solar poles shows striking differences with that observed near the ecliptic plane. By sampling these energetic particle compositions, both elemental and isotopic, with greatly increased precision, we can systematically investigate and interpret these abundance differences, and identify others that have to date remained beyond the reach of experimental study.

This paper describes the Ultra Low Energy Isotope Spectrometer (ULEIS), one of the 4 advanced mass spectrometers for the ACE mission that, as a group, cover the range from solar wind (1 keV nucl^{-1}) energies to galactic cosmic rays (100–1000 MeV nucl^{-1}), thereby allowing a global investigation of these different energetic material samples (Stone et al., 1989). ULEIS operates in the energy range from $\sim$45 keV nucl^{-1} to a few MeV nucl^{-1}, thereby sampling particles from the sun, from interplanetary shock accelerated material, and from the interstellar neutrals accelerated at the termination shock. Since the scientific investigations to be undertaken with ULEIS are coordinated with the other ACE instruments, other papers in this issue contain discussions that deal with the issues discussed below (Gloeckler et al., 1998; McComas et al., 1998; Möbius et al., 1998; Stone et al., 1998b) .

1.1. ELEMENTAL AND ISOTOPIC COMPOSITION OF MATTER

The bulk of our knowledge of solar system abundances derives primarily from studies of terrestrial and meteoritic material (Anders and Ebihara, 1982). Compilations of these abundances serve as a baseline for a broad range of astrophysical, solar, and planetary studies. Improving our knowledge of the elemental and isotopic abundances solar system reservoirs is therefore of fundamental importance.

1.1.1. *Solar Isotopic Abundances*

Spectroscopy of solar emission lines has long been used to study the *elemental* composition of the sun, but this technique is not effective in determining *isotopic* abundances. However, shock waves in the solar corona routinely accelerate material to high energies; these particles often escape into the inner solar system where they can be studied in detail. These isotopic measurements are sufficiently difficult that only a handful of such particle events have been studied, and these with limited statistical accuracy (Mewaldt and Stone, 1989; Selesnick et al., 1993). For C, N, O, and Mg, isotopic abundance measurements to date are all consistent with solar wind (where available) and meteoritic abundances (Mewaldt and Stone, 1989). On the other hand, the first measurements of ^{22}Ne/^{20}Ne showed a significant (factor of 2) excess abundance of ^{22}Ne, while more recent results from SAMPEX show ^{22}Ne/^{20}Ne similar to solar wind values as might be expected (Selesnick et al., 1993). These differences might be due to differences between individual solar particle events. By measuring solar isotopic abundances in a large number of particle events, it will be possible to characterize the event-to-event variations, and correct for systematic trends.

1.1.2. *Coronal Composition*

Material in the solar corona originates from the photosphere of the sun, moving outwards by poorly understood processes. Recent evidence from the Ulysses solar wind measurements (Galvin et al., 1984, 1995) shows that the long-known first ionization potential (FIP) enhancements observed in the ecliptic plane are largely reduced or absent altogether in the fast solar wind observed over the solar polar regions. This gives evidence for the importance of magnetic fields in the operation of an ion-neutral separation process that causes the FIP bias (von Steiger and Geiss, 1989; Fisk et al., 1998). Large (‘gradual’) solar particle events appear to accelerate material over large regions of the corona itself or regions close to the sun (Mason et al., 1984; Reames et al., 1996). Thus, the elemental composition of solar energetic particle nuclei in gradual events also carries information about the coronal composition. At higher energies (10 s of MeV nucl^{-1}) there are systematic abundance variations from photospheric values that correlate well with particle charge-to-mass ratio (Breneman and Stone, 1985). As shown in Figure 1, for particles of energies near 1 MeV nucl^{-1} and below, these deviations are smaller (Mazur et al., 1993). By studying the abundances over a broad energy range, it is

possible to construct a table of coronal abundances from the energetic particle population, for comparison with abundances obtained from solar wind measurements and photospheric spectroscopy.

1.1.3. *Corotating Interaction Regions and Pickup Ions*

High speed solar wind streams emanate from magnetically open portions of the corona, and in the solar ecliptic plane these regions typically alternate with regions of closed coronal magnetic field lines that are associated with the source of 'slow' solar wind. Under solar minimum conditions, when other activity on the sun is relatively low, the high and low speed streams can continue for months, setting up nearly steady state in the inner heliosphere. In these situations, the high speed solar wind streams overtake the slow wind, and interact so as to form forward and backward moving shock waves (Barnes and Simpson, 1976; McDonald et al., 1976). This interaction is strongest at radial distances of a few AU, and since the regions appear to co-rotate with the coronal features that are the origin of the fast and slow wind, they are called 'co-rotating interaction regions' (CIRs). Ions energized in these regions flow into the inner heliosphere, and can be observed near Earth (Mewaldt et al., 1978; Gloeckler et al., 1979; Richardson and Hynds, 1990). Comparison with recent solar wind abundance determinations shows that the CIR abundances at 1 AU are close to the *average* between fast vs slow solar wind, as shown in Figure 2 (Mason et al., 1997). In addition, some CIR elemental abundances such as C show a dependence on solar wind speed which is not expected from models developed to date (Fisk and Lee, 1980). It may be that in addition to a solar wind source, CIRs also accelerate other low energy components in the interplanetary medium, such as pickup ions. Pickup ion sources include interstellar neutrals, and products from the sputtering and evaporation of interplanetary dust, and so these studies may yield new insights into other material in the interplanetary space (Gloeckler et al., 1994).

1.1.4. *Anomalous Cosmic-Ray Composition*

Anomalous cosmic rays (ACR) arise from interstellar neutrals of high ionization potential that enter the heliosphere, are ionized by solar UV or charge exchange, and then transported outwards again to the termination shock region where they are energized to $\sim$10 MeV nucl^{-1} (Fisk et al., 1974; Pesses et al., 1981; Klecker, 1995; Cummings and Stone, 1996). Recent observations from SAMPEX of a transition from singly ionized Oxygen to multiply charged Oxygen near 20 MeV nucl^{-1} (Mewaldt et al., 1996; Klecker et al., 1997) have revealed the overall energy limits of the anomalous cosmic-ray acceleration mechanism (to $\sim$240 MV/Q), and have put estimates of the time scale for acceleration ($\sim$1 year) on a firmer basis (Jokipii, 1996). The ACR thus provide a sample of the neutral gas in the local interstellar medium. Although the elemental abundance of the ACR shows extreme fractionation (hence the name), the isotopic ratios should be relatively little affected by the acceleration process. Thus studies of the ACR isotopic composition can be

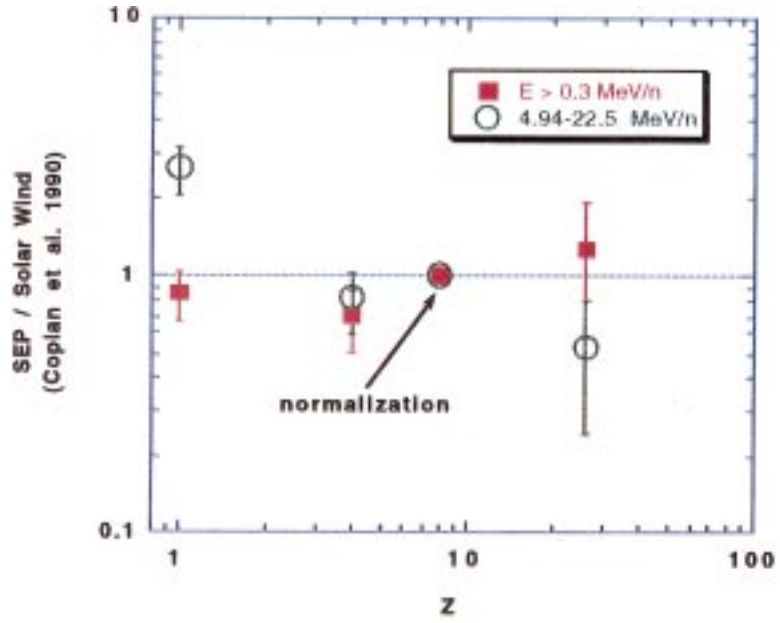

Figure 1. Abundances measured in 10 large solar particle events compared to solar wind abundances. Note that for abundances averaged over E > 0.3 MeV nucl^{-1}, there is little difference from solar wind abundances, while for the same particle events, the abundances for 4.9–22 MeV nucl^{-1} show significant differences from the solar wind (Mazur et al., 1993).

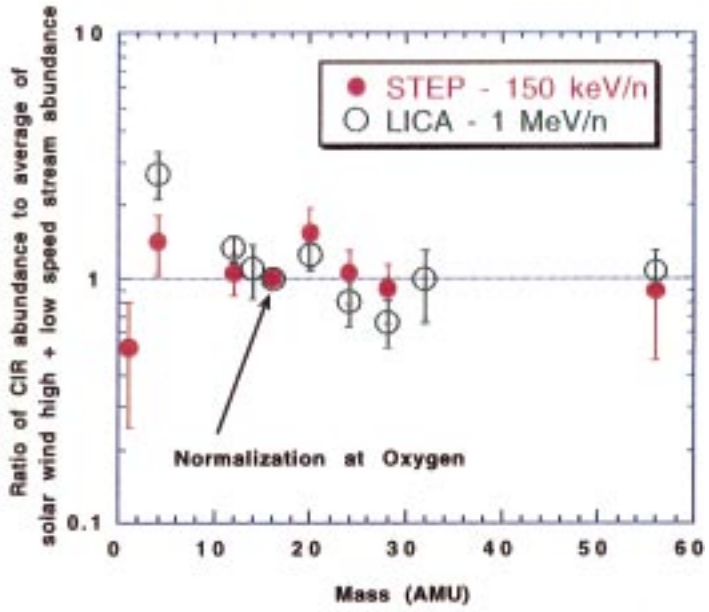

Figure 2. Comparison of CIR element abundances at 150 keV nucl^{-1} and 1 MeV nucl^{-1} with the average of *Ulysses* fast and slow speed solar wind composition (Mason et al., 1997).

used as a new tool to determine local galactic isotopic composition. Since ACR fluxes are very low, instrumental studies to date have not had sufficient precision to determine the isotopic ratios with sufficient detail to reveal anomalies (if any) with solar system abundances (Mewaldt et al., 1976).

1.2. Particle acceleration on the Sun and in the heliosphere: models

In addition to measurements of the abundances of particles in large solar particle events and in impulsive solar flares, the distribution of particles with energy is an important diagnostic of the acceleration and transport processes. An acceleration model not only must account for the observed elemental and isotopic abundances, but it also must describe how the energy is distributed via electric and magnetic fields among ions with differing mass to charge ratios. The energy spectra are key to our understanding of how these samples of solar material become energized and how they propagate to the observer.

1.2.1. *Energy Spectra of Large Solar Particle Events*

Large solar particle events have been observed in interplanetary space simultaneously with several spacecraft; these observations, together with the association of the events with interplanetary Type II radio bursts indicate that a traveling interplanetary shock accelerates the particles, possibly out of the ambient solar wind. Included in this seed population might also be a contribution from interstellar pickup ions (Gloeckler et al., 1994). Figure 3(a) shows the energy spectra of several particle species measured in a single solar energetic particle event (Mazur et al., 1992). The solid curves are fits to the data using a model of stochastic particle acceleration that might occur at such a shock. Figure 3(b) shows the abundance ratios as functions of energy for the same event; the trends with energy indicate that the acceleration process is more efficient for particles with lower energies and lower mass to charge ratios.

The spectra in Figure 3 represent an average of the particle intensity over a several day-long time period. An alternative method shown in Figure 4 (Reames et al., 1997) measures the low energy particle spectra in the event's decay phase after the shock has traveled past the observer. In the region downstream of the shock, the spectra continue to rise as power laws at the lower energies, in agreement with the predictions of shock acceleration. These two examples of large solar particle event spectra illustrate the importance of measuring the spectra over a wide energy range for many particle species. They not only show how the acceleration process might favor one species over another, but they also shed light on the most appropriate way to use the spectra as a diagnostic of an acceleration process that evolves with time as the shock propagates out from the sun.

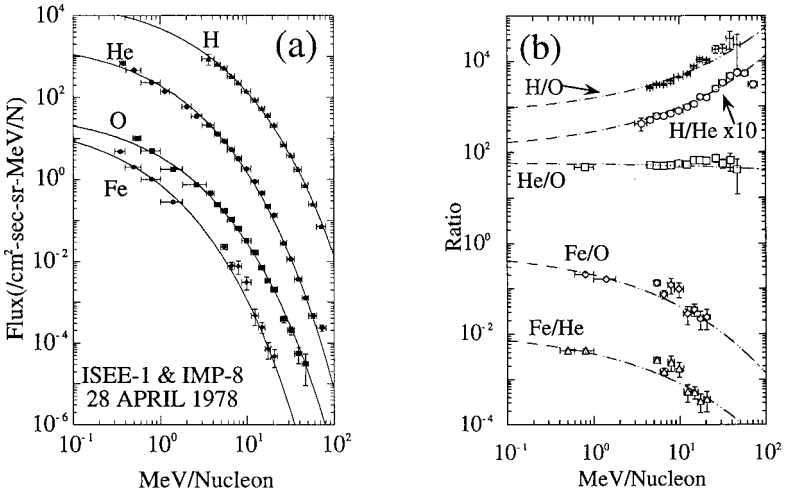

Figure 3. (a) Energy spectra of H, He, O, and Fe ions in a large solar particle event (Mazur et al., 1992). Solid curves are fits to a model of stochastic particle acceleration. (b) Abundance ratios as functions of energy from the same event. The systematic trends with energy suggest that the acceleration mechanism is more efficient for particles with lower energy and smaller mass to charge ratios.

1.2.2. *Energy Spectra of Impulsive Solar Flares*

Impulsive solar flares produce bursts of ∼100 keV electrons that stream along the magnetic field lines from the sun, as well as a charged particle population that is distinct from any other sample of matter in the heliosphere. These particle events, which typically last a few hours to a day, are enhanced in the ^{3}He isotope by a factor of 10^3–10^4 when compared to the composition of the solar corona. Compared to Oxygen, the elements Neon through Sulfur are also enhanced, but by a comparatively small factor of 3–5; Iron is more abundant by a factor of ∼10. Isotopic anomalies in ^{3}He-rich flares have been observed only once, during a single series of events in July 1992; these events showed modest enhancements in neutron-rich isotopes of Neon and Magnesium (Mason et al., 1994). Impulsive flares particles also exhibit high ionization states (Luhn et al., 1985) and are also associated with non-relativistic electrons (Reames et al., 1985), indicating that these particles are likely a direct sample of the material that is accelerated at the flare site in the corona.

In the initial work on this subject, the most successful mechanism that accounted for the high abundance of ^{3}He used a plasma resonance method to preferentially heat the ^{3}He (Fisk, 1978), which has a unique charge to mass ratio. After the preheating, a second stage acceleration by stochastic processes (Möbius et al., 1982) predicted rounded spectra at the lowest energies; this is in contrast to the observed spectra shown in Figure 5. The trend for the energy spectra to continue to rise even at energies near 20 keV nucl^{-1} suggests that the low energy particles contribute significantly to the total energy released in the flare. These are energies

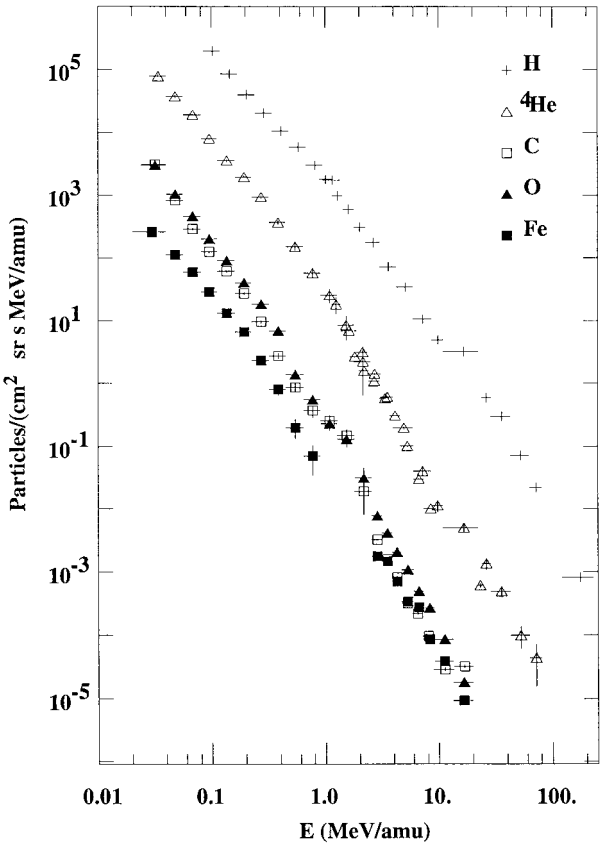

Figure 4. Gradual solar particle event spectra measured by the EPACT instrument on the WIND spacecraft down to ∼20 keV nucl^{-1} (Reames et al., 1997) during 21–25 October 1995. The low energy portions of the spectra were accumulated after an interplanetary shock passed the spacecraft on 22 October.

well below those probed by gamma-ray observations in flares (Ramaty et al., 1995). More recent theories using cascading plasma waves (Miller and Reames, 1995; Miller, 1998) are still being developed, but promise to account for the abundance anomalies in both elements and isotopes as well as the shape of the energy spectra.

2. Design Requirements

As the preceding discussion has shown, critical new information about the origin and evolution of the solar system and local galactic region can be obtained from high resolution elemental and isotopic composition of energetic particles from matter reservoirs on the solar corona, the solar wind, the local interstellar gas, and, perhaps, interplanetary dust. Elements over the range He to the Fe group are well suited for this study since they comprise the bulk of the material heavier than

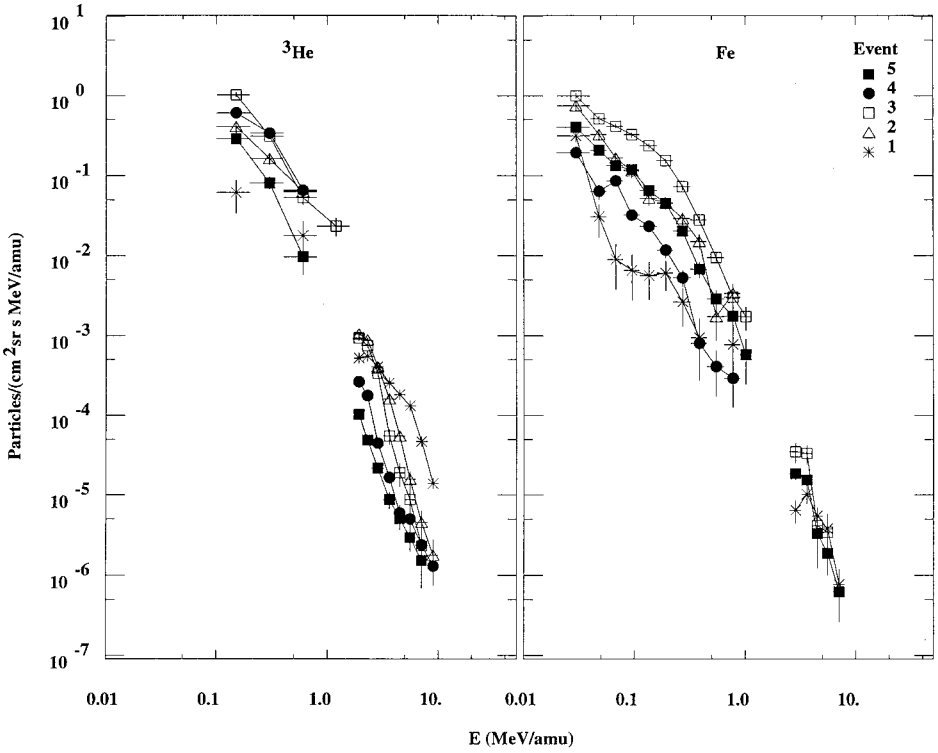

Figure 5. Impulsive flare energy spectra measured in five events by the EPACT instrument on the WIND spacecraft (Reames et al., 1997). Ions are accelerated beyond 10 MeV nucl^{-1}, and the spectra continue to rise at the lowest measured energies. Both the upper and lower observed energies, as well as the spectral forms, place tight constraints on the particle acceleration mechanism.

protons, and are the tracers of the primary nucleosynthetic processes that formed the solar system.

2.1. TELESCOPE

The Ultra Low Energy Isotope Spectrometer (ULEIS) for the ACE mission is one of a suite of high resolution spectrometers designed to give coordinated observations over the range of energies beginning at the solar wind ($\sim$1 keV nucl^{-1}) and extending up to moderate energy galactic cosmic rays (several hundred MeV nucl^{-1}). This broad energy range encompasses a huge dynamic range of flux levels (about 19 orders of magnitude) and time variations, and requires multiple techniques to span the entire range. ULEIS covers a range intermediate between the solar wind (SWIMS and SWICS) instruments (Gloeckler et al., 1998), and the solar isotope spectrometer (SIS) instrument (Stone et al., 1998b) – i.e., from about 45 keV nucl^{-1} to a few MeV nucl^{-1}. Exploratory measurements of ultra-heavy

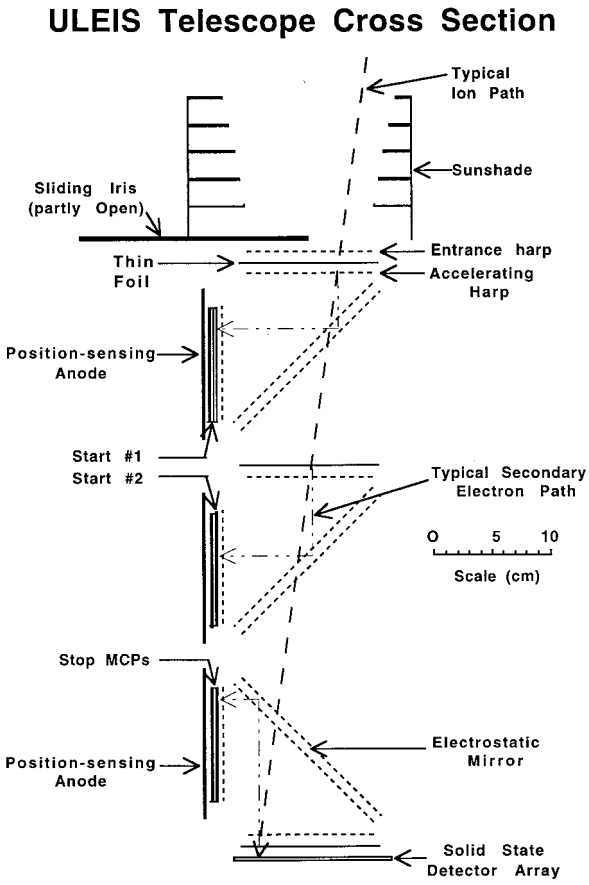

Figure 6. A cross sectional view of the ULEIS telescope.

species (mass range above Ni) will also be performed in a more limited energy range near 0.5 MeV nucl^{-1}.

In the ULEIS energy range the particle sources available for study include: solar energetic particles, particles accelerated by interplanetary shocks including Coronal Mass Ejection (CME) events, CIR ions, and anomalous cosmic rays. Fluxes in this range cover about 9 orders of magnitude from a large interplanetary shock to quiet periods when anomalous cosmic rays dominate. The isotopic abundances in these particle sources are expected to be close to solar or meteoritic values, which is to say that the main isotope peaks can be 50–100 times the abundance of the adjacent rarer isotopes. Making statistically significant determinations of the rare isotope abundances requires both high mass resolution ($\sigma_M \sim 0.2$ amu) and low background. In addition, substantial data rates are required since resolution of the rare isotope peaks is sufficiently difficult that it must be done on the ground. This means that for each rare isotope event detected, large numbers of a nearby common isotope must be telemetered, since the on board instrument data processing unit

TABLE I
ULEIS design goals

	Goal	Science driver
Geometric factor	1 cm^2 sr	adequate counting statistics for – small particle events – anomalous cosmic rays
Particle species measured	$2 \leq Z \leq 28$	– He–Ni covers most abundant material – main nucleosynthetic sequence
Elemental energy range	0.3–2.0 MeV/n	– large solar particle events – impulsive solar flares; – interplanetary shocks – corotating interaction regions
Mass resolution	$\sigma_m < 0.15$ amu ($Z = 6$)	– resolve adjacent isotopes for C-Si
	$\sigma_m < 0.5$ amu ($Z = 26$)	– even isotopes for heavier nuclei
Event rate range, R	1/week $< R < 10^5$ s^{-1}	low background to cover – anomalous cosmic rays – high event rate in large solar particle events

is unable to separate adjacent isotopes for elements heavier than helium. Table I summarizes key design goals for ULEIS, and lists the primary scientific goals that lead to those requirements.

2.2. DATA PROCESSING UNIT

The ULEIS telemetry bit rate is limited to approximately 1 kb s^{-1}, which is insufficient to transmit detailed data on all particles triggering the telescope. In order to follow, e.g., anisotropies and the evolution of particle spectra during intense periods, particles need to be identified in broad mass and energy bins and counted in so-called 'matrix-rates'. The low triggering efficiency of the telescope for protons and helium is helpful in this regard; in addition, when counts become too high, there is a closable cover that is activated to shield the telescope aperture and thereby lower the triggering rate. In order to count all particles for binning the matrix rate processing must be able to handle up to $\sim$3000 counts s^{-1}.

Figure 7. The ULEIS instrument shown with the telescope on its mounting bracket, and connected to the analog electronics and DPU boxes.

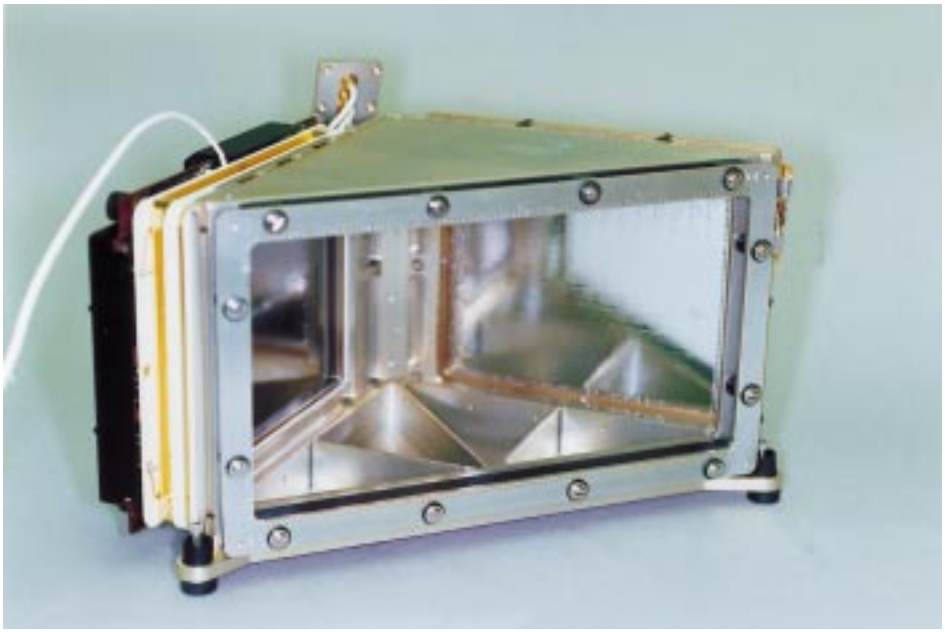

Figure 8. A single 'wedge' assembly consisting of thin foil, electrostatic mirrors, and microchannel plate assembly. The view is through the electrostatic mirror.

TABLE II
ULEIS telescope typical energy ranges

	Energy ranges (keV nucl^{-1})					
	$\sigma_m < 0.3$ amu		$\sigma_m < 0.6$ amu		$\sigma_m < 2$ amu	
Species	Lo[a]	Hi[b]	Lo[a]	Hi[b]	Lo[a]	Hi[b]
^{4}He	90–2000	197–8100	65–2000	197–8100	55–2000	197–8100
^{12}C	120–770	154–13300	78–770	105–13300	42–770	105–13300
^{16}O	153–620	180–7250	90–620	105–10000	45–620	87–10000
^{28}Si	280–405	290–2300	146–405	153–5700	50–405	58–5700
^{56}Fe	–	–	–	270–2360	80–220	82–3015

[a]Small solid-state detectors (D1-D4).
[b]Large solid-state detectors (D5-D7).

3. Instrument Description

3.1. Operating principles

A cross section of the ULEIS telescope is shown in Figure 6, and typical energy ranges are summarized in Table II. The telescope box is mounted on a bracket (see Figure 7) so that its view cone points in the sunward hemisphere at an angle of 60° to the ACE spin axis. The instrument is a time-of-flight mass spectrometer that identifies incident ion mass and energy by simultaneously measuring the time-of-flight, τ, and residual kinetic energy, E, of particles that enter the telescope acceptance cone and stop in one of the array of seven silicon solid-state detectors (SSDs) in the back of the telescope. The time-of-flight is redundantly determined by two start pulses, START-1 and START-2, and a STOP pulse from 'Z-stack' microchannel plate (MCP) assemblies that detect secondary electrons that are emitted from the thin foils when the ion passes through them. These secondary electrons are accelerated to ~1 kV and deflected onto the MCPs by electrostatic mirrors. The design of the secondary electron optics yields isochronous flight paths for all secondary electrons emitted normally from the foil or detector surface. The measured energy, $E = \frac{1}{2}mv^2$, and the velocity, $v = L/\tau$ (where L is the path length in the telescope), are combined to yield the mass of the ion,

$$m = 2E\left(\frac{\tau}{L}\right)^2 , \tag{1}$$

and the energy per nucleon, E/m, inside the telescope. The ion incident energy is obtained after correcting for the energy loss in the foils and the front contact of the solid-state detector. ULEIS measures only the mass of the incident particles, and so cannot distinguish isomers such as ^{40}Ca and ^{40}Ar. However, for isotopes lighter than Ni, there are only a few such isomers, and in all cases for solar-system abundances, one isotope has the dominant abundance (Anders and Ebihara, 1982),

so this is not an important source of ambiguity in the data. The design of ULEIS evolves from consideration of a number of important scientific goals for particle measurements on the ACE mission. First is the need to measure a large number of isotopes over a broad energy range for solar and interplanetary particle populations. Second is the requirement to perform accurate measurements over a wide dynamic range of particle intensities, e.g., from intense solar particle events and strong shock events to small, ^{3}He-rich flares that are near the threshold of sensitivity for previous instruments. Third is the requirement to operate reliably over a multi-year lifetime. These considerations require an ion detector whose design achieves a low energy threshold, high mass resolution, and large geometrical factor, and that employs technologies of proven long-term performance on spacecraft. The low energy threshold is achieved by using the time-of-flight technique with a thin entrance foil on the telescope. The high mass resolution is attained by combining time-of-flight measurements of high accuracy ($<$300 ps FWHM) with a long ($\sim$50 cm) flight path whose length is determined accurately by measuring the (x, y) positions where the ion penetrates each of the three thin foils. Finally, the large geometrical factor is obtained by using large-area microchannel plates (8 cm $\times$ 10 cm) and an array of solid-state detectors with total area of $\sim$73 cm^2. ULEIS has a full instrument geometrical factor of $\sim$1.3 cm^2 sr with 100% duty cycle for all species.

3.2. TELESCOPE SCHEMATIC

This section describes details of the telescope components, starting at the top of Figure 6 and moving towards the bottom.

3.2.1. *Closable Cover*

Solar ultraviolet radiation may cause secondary electron emission from the telescope foil, thus increasing the background in the instrument. The ULEIS design avoids this by pointing the telescope at 60° to the spin axis and including a sunshade that prevents sunlight from striking the foil. Since the ACE spin axis is maintained pointing directly at the sun (Chiu et al., 1998), the ULEIS field of view scans a band in the sky perpendicular to the ecliptic. The ULEIS sunshade serves a secondary role by preventing particles incident from outside the instrument view cone from striking the front foil, thereby significantly lowering the peak START-1 count rate in intense solar flare or interplanetary shock events. However, in some events, the ULEIS front foil count rates could exceed $\sim 5\times10^6$ s^{-1}, thereby causing accidental triggering in the time-of-flight system and pulse pile up in the solid-state detectors.

To prevent this, a mechanical shutter ('sliding iris' in Figure 6) slides closed under on-board control depending on the START-1 MCP singles counting rate. The iris is controlled by a Clifton size 11 stepper motor, and has four discrete settings corresponding to 100%, 25%, 6%, and 1% of full opening, thereby making it possible for ULEIS to operate in the most intense events with excellent mass resolution. The four iris settings are sensed by Optek optical switches. If the iris

is positioned at some other intermediate location, the optical switches provide no information on the location. However, in this case the cover can be reset by ground command, and its location determined by counting motor steps. The 6% and 1% settings of the iris are achieved using holes in the iris cover itself, and so are not dependent on precise mechanical location of the cover. The iris is tightly closed at launch to provide an acoustic seal; release post-launch is done with redundant miniature wire cutters and springs.

Even when the geometrical factor is reduced by the iris, in intense events ULEIS will record sufficient events to completely fill its allocated telemetry, and so statistical accuracy will not suffer. Changing of the iris position takes place only on boundaries of the instrument's internal collection cycle, in order to prevent data being taken in an intermediate state. An encoded set of light-emitting diodes on the iris provides positive feedback to the control circuitry that the desired setting has been reached. Two radioactive sources are located on the inside of the iris cover in order to permit in-flight calibration when the cover is closed: 1 μCi of ^{244}Cm (18 year half life; 5.80 and 5.76 MeV alphas), and 0.3 μCi of ^{148}Gd ($\sim$35 y half life; 3.2 MeV alpha).

Behind the sliding iris but in front of the entrance thin foil, there is a single entrance 'harp' assembly (see Section 3.2.2) held at ground potential, in order to electrostatically shield the entrance foil that is at a negative HV potential.

3.2.2. *Wedges*

The telescope's three timing signals (START-1, START-2, and STOP) each originate from modular assemblies called 'wedges' due to their triangular shape. Figure 8 shows a single START wedge assembly. The three 'active' surfaces of each wedge consist of a thin foil, an electrostatic mirror, and a microchannel plate assembly (see also Figure 6). In order to have the signal output of the microchannel plate assemblies at ground potential, the wedge is biased with the foil at negative HV (typically -4000 V). Electrons emitted from the inner surface of the foil are accelerated towards the accelerating harp, which is biased at about -3000 V. They then enter a uniform potential region bounded by the accelerating harp, inner electrostatic mirror harp, and a harp in front of the microchannel plates. The outer electrostatic mirror harp is at ground potential. Secondary electrons coast in the uniform potential region, entering the electrostatic mirror where they are reflected 90°, and re-emerge moving towards the microchannel plates. After passing through another harp in front of the MCPs, they strike the front surface of the MCP. The MCP front surface is biased at about 50 V more positive than the uniform potential region, in order to reduce background.

Each harp is strung with 0.001″ stainless steel wire with 1.0 mm spacing, for a net transparency of 97.5% for harps perpendicular to the telescope boresight, and 96.4% for the mirror harps at 45° to the telescope axis. The transparency of the 3 harps in each wedge assembly is thus $0.975 \times 0.964 \times 0.964 = 0.906$. The harp transparency is combined with foil transparency in cumulative fashion in Table III.

TABLE III
ULEIS telescope transparency budget

Element	Transparency	Cumulative transparency
Entrance harp	0.975	0.975
START-1 foil mesh	0.937	0.914
START wedge harps	0.906	0.828
START-2 foil mesh	0.937	0.776
START wedge harps	0.906	0.703
STOP wedge harps	0.906	0.637
STOP foil mesh	0.937	0.596
Total		0.596

Since multiple secondary electrons are emitted by particles heavier than He over the ULEIS energy range, the harps (including the one in front of the MCPs) have very low probability of stopping all the electrons emitted by passage of a single ion.

The design of the mirrors and mounting pieces was optimized to prevent fringe fields from distorting the flight paths of the secondary electrons. The spacing of acceleration regions between the thin foil and the accelerating harp, and in between the 2 harps in the electrostatic mirror is 1.0 cm, which is 10 times the harp wire spacing. The mirror assemblies used in ULEIS are based on smaller designs developed for use in low energy nuclear accelerators (Starzecki et al., 1982). These smaller systems have estimated intrinsic time dispersions of $\sim$115 ps for fission fragments (Starzecki et al., 1982). Timing performance data for the ULEIS wedges is presented in Section 4.2.

3.2.3. *Foils*

The ULEIS START-1 foil is a 2000 Å thick polyimide foil, coated on both sides with 300 Å of Al, supplied by Luxel Co., of Friday Harbor, Washington (Powell et al., 1997). The double coating prevents pinholes in the Al on one side of the foil from letting scattered light into the telescope chamber. The sunshade, along with the telescope bracket angle of $\sim 60^\circ$ to the solar direction, ensure that direct sunlight never strikes the START-1 foil. Omnidirectional Lα backscattered UV is a potential concern with thin foils exposed to a large solid angle of sky. However, for typical interplanetary UV levels as measured on the Pioneer–Venus probe (Ajello, 1990) the ULEIS start foil is sufficiently opaque to limit counting rates due to this source to less than a few hundred per second (Postlaunch note: the actual START-1 count rates observed shortly after full bias was applied were about 2000 counts s^{-1}

TABLE IV
Material in front of ULEIS solid-state detectors

Element	Material	Thickness (Å)[a]	Thickness (μg cm^{-2})
START-1 foil outer Al layer	Al	325 ± 32	8.8 ± 0.9
START-1 foil substrate	polyimide	2075 ± 100	22.8 ± 1.1
START-1 foil inner Al layer	Al	300 ± 30	8.1 ± 0.8
START-2 foil substrate	polyimide	2175 ± 100	23.9 ± 1.1
START-2 foil Al layer	Al	300 ± 30	8.1 ± 0.8
STOP foil Al layer	polyimide	287 ± 28	7.7 ± 0.8
STOP foil substrate	Al	2185 ± 100	24.0 ± 1.1
Solid-State Detector front contact (average)	Al	2000 ± 1000	54.0 ± 27.0
Total			157.5 ± 33.5[b]

[a]Manufacturer's specifications.
[b]Comprised of polyimide and Al absorbers.

for the START-1 time-of-flight discriminator, and 5000 counts s^{-1} for the START-1 WSA electronics). The START-2 and STOP foils are 2000 Å thick polyimide, with a single 300 Å Al coating on the side of the foil facing into the wedge. A complete list of absorbing material in front of the solid-state detectors is given in Table IV.

The foil thickness is chosen to be the minimum consistent with sufficient mechanical strength to survive launch acoustics and vibration. All the foils are mounted on a double mesh combination consisting of a custom-etched Au plated Be–Cu mesh with wire thickness of 0.005″, and line spacings of 4.0 lines per inch (transparency 96%). On this mesh, a second, fine mesh (0.0015″ wires, 16 lines per inch) is mounted along with the foil (transparency 97.6%). The transparency of the two meshes is 0.937 (see Table III). The Be–Cu mesh is nearly mechanically decoupled from its mounting frame by means of thin attachment prongs that are highly compliant. This mesh then 'floats' within a restraining frame so that flexing of the wedge assembly is not transmitted directly to the foil mesh. The wedges themselves are mechanically decoupled from the rest of the telescope via attachment points solely at the base of the telescope box. To provide protection against severe acoustic levels at launch, the 'sliding iris' cover is closed securely during launch, and opened with redundant squibs at a later time. The sliding iris cover itself, as well as the walls of the telescope box, were thickened to provide additional acoustic shielding. To provide for rapid venting of the telescope chamber during launch ascent, without at the same time allowing significant acoustic energy into the telescope chamber, the telescope chamber is vented through a 'muffler' tuned to dampen at frequencies near the peak of the acoustic spectrum.

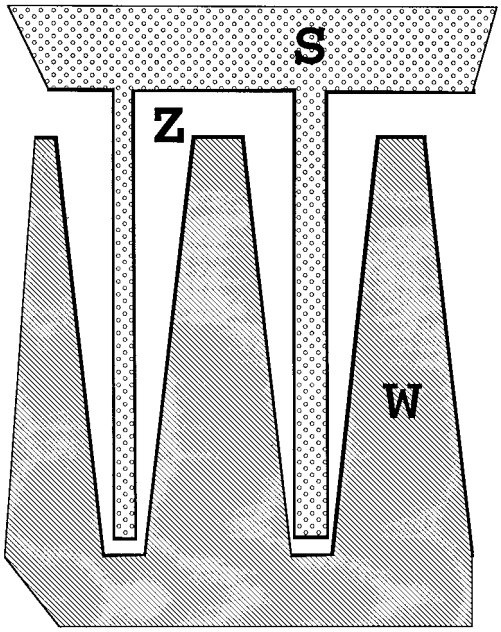

Figure 9. 'Wedge and strip' anode schematic.

3.2.4. *MCP Assemblies*

Each MCP assembly consists of three microchannel plates in a 'Z-stack' configuration, which was chosen to optimize signal FWHM and timing (Siegmund et al., 1986b). The plate size is 80×100 mm, with 1 mm thickness, 25 μm pore size, and 19° bias angle. The nominal gain is 5×10^6 at 3000 V/set, with a leakage current range of 10–25 μA/plate at 1000 V bias. Each Z-stack was procured (from Galileo Electro-Optical, Inc.) as a matched set, and the three plates were mounted directly in contact with each other, without interplate spacers or contacts. The electron cloud output from the last plate in each stack is collected by the wedge-and-strip anode, which was placed 1.0 cm in back of the plate in order to allow the electron cloud to spread.

Achieving uniformity of response over the entire area of these large MCPs is important for high performance operation of the system. The combination of large area and thin (1 mm) plate diameter can lead to large differences in response due to deviations in the plates from strict flatness. Since the plates are held together at the edges, deviations from flatness tend to occur towards the center of the plates. Where the plates are no longer touching each other, the gain is larger since the electron cloud can spread out between adjacent plates, thus triggering more channels deeper in the stack than would be the case if the plates were rigidly held together. This leads to an apparent decrease of gain (by a factor of $\sim$5) in the outer portion of each MCP stack. For the ULEIS flight instrument, the orientations of the individual MCPs in each Z-stack were selected in order to achieve a nearly uniform response

to a UV source (by Siegmund Scientific, Berkeley, CA). After launch, the plates may change their 'flatness' over time due to outgassing of water, and in response to stresses within the stacks themselves. This may degrade the timing performance of the system, although the constant-fraction discriminators in the time-of-flight electronics should help minimize these effects.

3.2.5. *Wedge and Strip Anode*

Electrons from the MCPs fall on three collector wedge-and-strip anodes (WSA) (Anger, 1966) supplied by Siegmund Scientific, Berkeley, CA. Figure 9 shows a sample three collector WSA (magnified) pattern where the regions marked W, S, and Z ('wedge, strip, and zigzag') are separate conductive regions (Lapington and Schwarz, 1986). For the ULEIS instrument, the anodes are applied with a thick film technique on a 1 mm thick alumina substrate with a pattern consisting of 30 cells covering an area 8.5 × 10.4 cm, with gaps between the anode elements of 0.002″. For electron cloud sizes larger than the individual scale sizes shown, the anodes collect a charge Q_W, Q_S, and Q_Z that can be analyzed to give the location of the centroid of the charge cloud. The pulse sizes on all three electrodes are analyzed and telemetered with each event. A rough, unscaled (x', y') location is then obtained from the equations:

$$x' = \frac{Q_S - X_{\text{talk}} Q_Z}{Q_W + Q_S + Q_Z} \tag{2}$$

and,

$$y' = \frac{Q_W - X_{\text{talk}} Q_Z}{Q_W + Q_S + Q_Z} \,, \tag{3}$$

where X_{talk} is a factor that corrects for some of the cross-talk distortions that arise due to capacitive coupling (few hundred pF typical) between the elements of the anode (Siegmund et al., 1986a). Calibrated locations on the anode are then obtained from Equations (2) and (3) by applying an offset from 0, a scaling factor, and then a final re-mapping that removes the residual distortions in the image. The (x, y) coordinate of the charge cloud center on the MCP has a one-to-one correspondence with the location where the ion penetrated the foils due to the simple reflective property of the electrostatic mirrors (see Figure 6). The overall accuracy of this technique locates the centroid of impact of the charge cloud on the anode to within a few mm, which exceeds the 1 cm accuracy needed to make path length corrections required for isotopic resolution (see Section 4.3.1.1).

3.2.6. *Solid-State Detectors*

The 8 × 10 cm active area at the back of the telescope is too large to be covered by a single, low noise solid-state detector. In order to avoid dead areas between the active elements, a custom layout was used, as shown in Figure 10. In order to cover the lower energy range of the instrument with very low noise detectors,

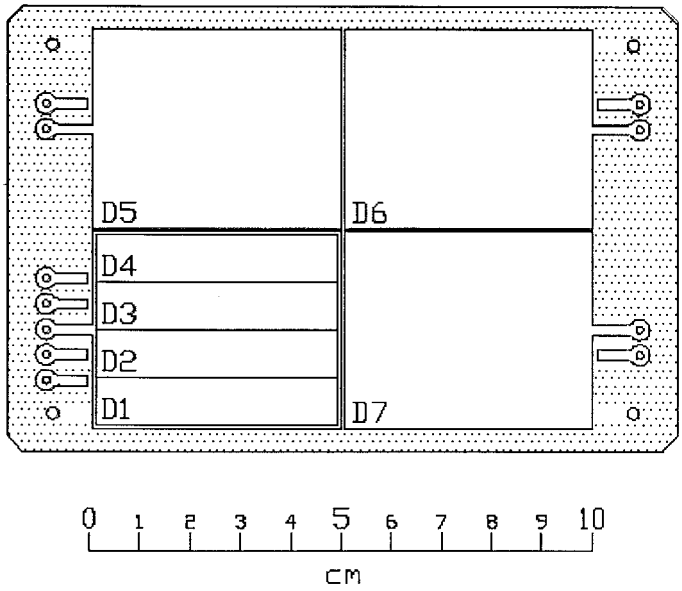

Figure 10. ULEIS solid-state detector array.

4 detector elements (D1, D2, D3, D4) in the array have 9.4 mm $\times$ 48 mm active areas, and three large elements (D5, D6, D7) have active areas of 38×48 mm. This arrangement covers over 90% of the nominal 80 cm^2 active area as determined by the MCP size. The silicon thickness for all elements is 500 ± 30 μm, and the metalizing on the active surface is 2000 ± 1000 Å Al. At nominal operating bias of 50 V, the alpha-peak FWHM is 25 keV for the small elements, and 45 keV for the large elements (typical). Leakage current at 50 V bias is typically 20 nA for the small elements, and 50 nA for the large elements. The detectors are mounted on a 0.080″ ceramic substrate. Signal leads were kept a minimum length by routing each detector signal through a pin that passes through the substrate and plugs directly into a circuit board that contains the 7 pre-amplifiers for the system. The detector assembly was provided by Micron Semiconductor, Inc., of Longwood, Florida.

3.3. FUNCTIONAL BLOCK DIAGRAMS

3.3.1. *Telescope Electronics*

Figure 11 is a block diagram of the ULEIS telescope box electronics showing the primary measurements and data flow. The selection of electronics located in the ULEIS telescope box is a compromise between the requirement for low-noise connections to the sensor, vs a requirement for low-temperature ($\sim$0 °C) operation of the solid-state detectors which limits the amount of power dissipation that can be tolerated in the telescope box itself. Relatively high power electronics such as the fast time-of-flight circuitry, are therefore located in a separate box (see below).

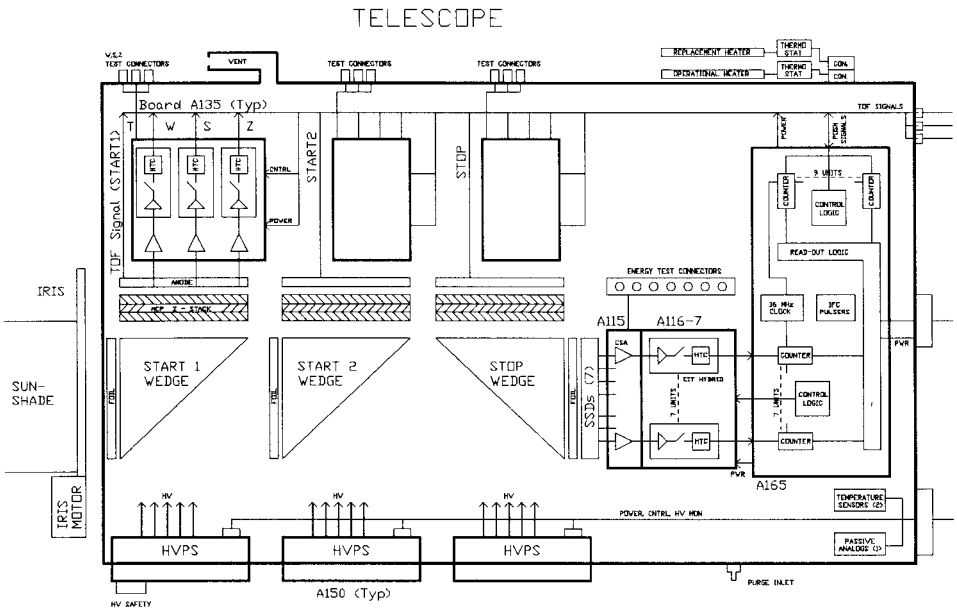

Figure 11. ULEIS telescope box block diagram.

Time-of-flight signals are routed directly from the telescope to the analog electronics box, (see below) where signals are examined to see if a valid stop has occurred (START-1 followed by a STOP within about 300 ns). If a valid stop occurs, then a signal is sent back to the telescope box to determine if one of the solid-state detectors has triggered in coincidence with the valid stop. If a coincidence occurs between the valid stop and a solid-state detector trigger, an event is recorded, consisting of the following information: energy deposit in the solid-state detector that was triggered; time-of-flight between START-1 and STOP (≡TOF-1), time-of-flight between START-2 and STOP (≡TOF-2), wedge (≡W), strip (≡S), and zigzag (≡Z) pulse sizes from the START-1, START-2, and STOP wedges, and status bits indicating which detector was triggered. These data are relayed to the data processing unit (DPU) for further processing (see below). Each event whose detailed pulse heights are telemetered is formatted into a 14-word event (1 word = 12 bits) whose contents are given in Table V. Four such events are telemetered each second.

3.3.1.1. *Wedge and strip anodes.* The three signals from the wedge, strip, and zigzag anodes are directed to a circuit board mounted directly in back of the anode. On this board, the three signals go through a single stage of wide dynamic range pre-amplification, and are then sent to hybrid circuits where they are digitized. The digital outputs are then sent to the analog electronics box (see below) for further processing. The hybrids used in ULEIS are a modification of the hybrids used in the ACE SIS and CRIS instruments, and were developed by the California

TABLE V
ULEIS telemetered PHA event contents

Word	Contents (12 bit words)
0	START-1 Wedge PHA
1	START-1 Strip PHA
2	START-1 Zigzag PHA
3	START-2 Wedge PHA
4	START-2 Strip PHA
5	START-2 Zigzag PHA
6	STOP Wedge PHA
7	STOP Strip PHA
8	STOP Zigzag PHA
9	SSD Energy
10	Time-of-flight 1 (START-1 - STOP)
11	Time-of-flight 2 (START-2 - STOP)
12	See below
13	See below

Normal Mode:

Word 12:	HAZ	LA1	LA0	SA1	SA0	D7	D6	D5	D4	D3	D2	D1
Word 13:	zero	zero	Event Box #						CO	ES	TOF2	TOF1
	MSB											LSB

Codes:
HAZ = Hazard flag.
LAn = Large solid-state detector address: 00 = D5, 01 = D6, 10 = D7, 11 = error.
SAn = Small solid-state detector address: 00 = D1, 01 = D2, 10 = D3, 11 = D4.
Dn = Discriminator number that fired.
Event box # = matrix rate box number assigned to this PHA event (6 bits).
CO = Calibrate/normal mode flag (1 = calibrate; 0 = normal).
ES = Energy system ID: 0 = large; 1 = small.
TOFn = which TOF system fired.

Calibrate Mode:

Word 12:	CE11	CE10	CE9	CE8	CE7	CE6	CE5	CE4	CE3	CE2	CE1	CE0
Word 13:	SSD ID			ES	CAL STEP			CM	CO	zero	TOF2	TOF1
	MSB											LSB

CE = Energy calibration step number.
SSD ID = Solid-state detector ID: 0 = D1, 1 = D2,. . . 6 = D7 (3bits).
CAL STEP = Time-of-flight calibration step number (3 bits).
CM = Calibrate mode speed (1 = slow).

TABLE VI
ULEIS energy and timing nominal specifications

System	Nominal specifications
Low threshold solid-state detector system	Detectors: 4×4.5 cm^2 500 μm thick detectors detector alpha peak = 25 keV FWHM Electronics: discriminator threshold 55 keV amplifier total energy range 55 keV–8 MeV analyzer: 12 bit height-to-time converter, 1 per detector
High threshold solid-state detector system	Detectors: 3×18.2 cm^2 500-μ thick detectors detector alpha peak = 45 keV FWHM Electronics: discriminator threshold: 500 keV amplifier total energy range 0.5–160 MeV analyzer: 12 bit height-to-time converter, 1 per detector
Time-of-flight system	Ranges: TOF-1: 5–335 ns; TOF-2: 5–210 ns discriminator: constant fraction analyzer: 12 bit successive approximation ADC, 1 per channel

Institute of Technology ACE group (Stone et al., 1998a, 1998b) Control circuitry for the hybrids resides in the back of the telescope box with the solid-state detector electronics.

3.3.1.2. *Solid-state detectors.* Solid-state detector signals are processed in a stack of 4 boards mounted directly in back of the detector array. The board closest to the array has preamplifiers for each of the 7 detectors. These signals are then processed in hybrid circuits mounted on the next two boards in the stack. The fourth board contains ACTEL CMOS field programmable gate array (FPGA) control circuitry for the solid-state detector hybrids, as well as for the hybrids on each of the wedge and strip anode circuit boards. The nominal thresholds and gains for the solid-state detectors are summarized in Table VI. The hybrids are Caltech hybrids similar to those used for the wedge and strip anodes.

3.3.1.3. *High voltage bias and miscellaneous.* The telescope box also contains three high voltage power supplies that are used to bias the foils, harps, and MCP assemblies (see Figure 11). The supplies are separately commandable in order to provide capability to bias microchannel Z-stacks of different initial gains, and to

TABLE VII
Singles event rates

Rate #[a,b]	Name	Logic[c]
0	D1	D1
1	D2	D2
2	D3	D3
3	D4	D4
4	D5	D5
5	D6	D6
6	D7	D7
7	START 1	START 1
8	START 2	START 2
9	STOP	STOP
10	Valid Stop 1[d]	VS1
11	Valid Stop 2[d]	VS2
12	Event	VS $*$ E $*$ / BUSY[e]
13	START 1 Wedge	START-1 (W + S + Z)
14	START 2 Wedge	START-2 (W + S + Z)
15	STOP Wedge	STOP (W + S + Z)

[a]Each rate is divided into 8 sectors per spin.
[b]Accumulation time: 24 s (2 spins).
[c]Discriminator output name shown; $*$ = logical AND; + = logical OR; / = logical NOT.
[d]Valid stop: START-n followed by a STOP signal within 300 ns.
[e]E = Solid-state detector trigger (any of D1 . . . D7).

allow for recovery of gain late in the mission in the event that prolonged radiation exposure decreases the output of the plates. To provide information on operating temperatures, four temperature transducers are placed at critical locations near the solid-state detector array, near the front of the telescope, in the solid-state detector electronics, and in the WSZ circuitry.

3.3.2. *Analog and DPU Electronics*

The remainder of the instrument electronics are housed in two separate boxes (see Figure 7). The analog electronics box contains the time-of-flight circuits, some control circuits for the telescope logic, and the low voltage power supply. Output from the analog electronics box is sent to the data processing unit (DPU), which formats the data for transfer to the spacecraft telemetry system. The DPU also processes commands and processes telescope pulse-height data for the matrix rates.

TABLE VIII
Example of ULEIS matrix rate bins

Energy nucl^{-1}	^{1}H	^{3}He	^{4}He	^{12}C	^{16}O	^{28}Si	^{56}Fe
20							20
28							
40				40	40	40	40
57		57	57				
80	75		80	80	80	80	80
113			113				
160	160	160	160	160	160	160	160
226			226				
320			320	320	320	320	320
453	453	453	453				
640			640	640	640	640	640
905			905				
1280	1280	1280	1280	1280	1280	1280	1280
1810			1810				
2560			2560	2560	2560	2560	2560
3620	3620	3620	3620				
5120			5120	5120	5120	5120	
7241			7241				
10240		10240	10240		10240		
13000	13000			13000			
Readout frequency (s)	12	12	12	24	24	24	24
Priority	2	3	3	4	4	4	5

Priorities rotate, so each species has highest priority depending on recent telemetry history; ‘background’ box is priority 1.

3.4. COUNT RATES

3.4.1. *Singles*

Counting rates of individual detector elements and various logic combinations are collected in 24-bit accumulators, and sectored into 8 sectors per spin. The rates are read out once for every two spins of the spacecraft (1 spin = 12 s). Table VII lists the singles rate definitions. All rates are compressed in the DPU before being telemetered.

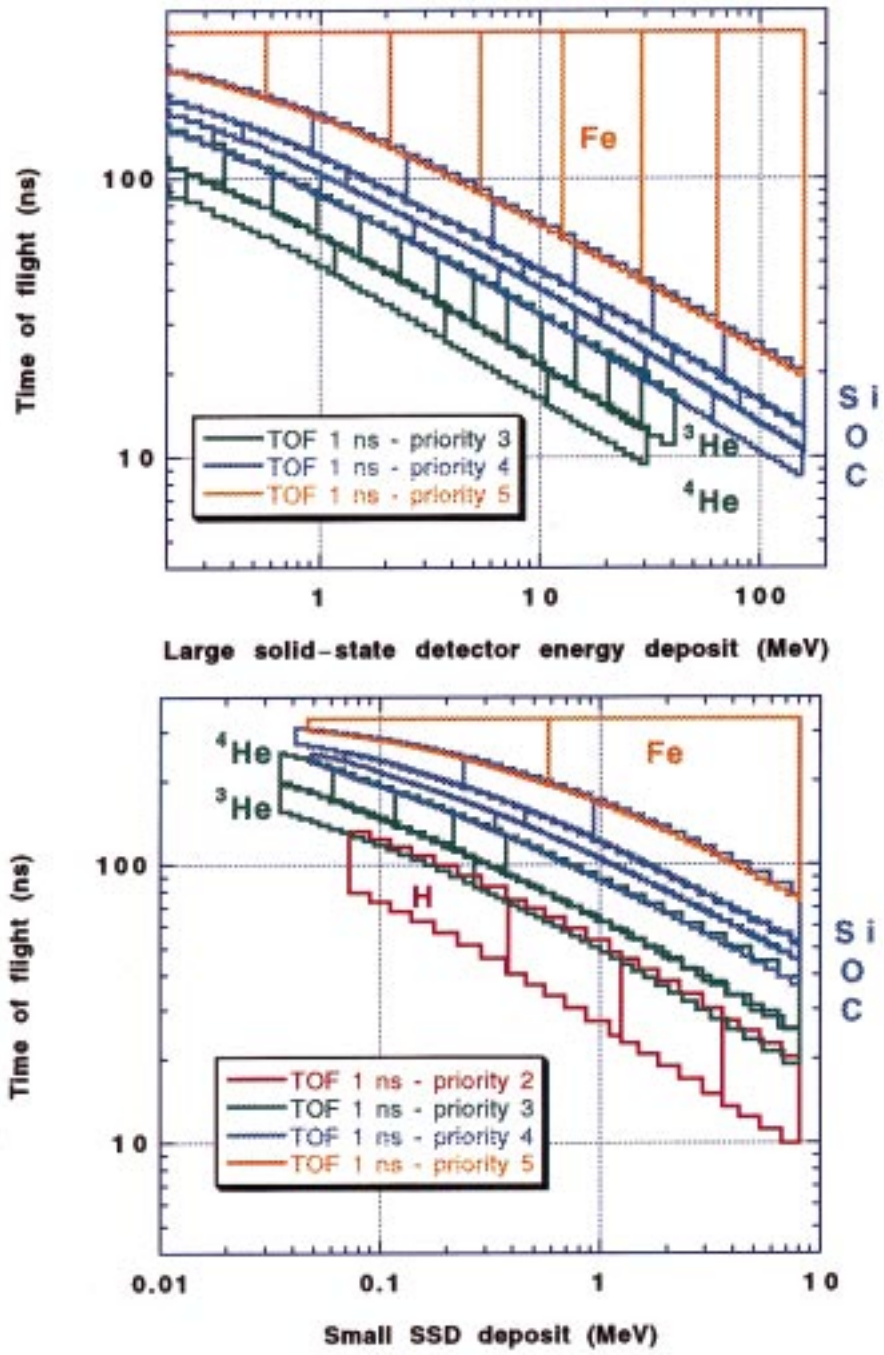

Figure 12. Example of ULEIS 'matrix rate' boxes in the time-of-flight vs energy matrices for both small and large solid-state detector systems (see also Table 7.)

3.4.2. *Matrix Rates*

Only a small fraction of the events triggering the telescope can be telemetered with complete pulse-height information. Therefore a second channel is used, consisting of matrix rates that assign individual events to species and energy boxes based on on-board processing of their pulse heights in the time-of-flight vs energy matrices. This processing takes place in the DPU. Table VIII shows an example of the types of coverage possible with this system, and Figure 12 shows locations of boxes in the time-of-flight versus energy matrices. The major species H, He, C, O, Si, and Fe each has assigned boxes, along with ^{3}He, which is important to monitor in small impulsive solar particle events. In the table, the entries show the boundaries of the boxes (start or stop energy per nucleon). The number of points in each spectrum varies from species to species. There are 34 matrix rates read out every spin (12 s), and 42 rates read out every 2 spins (24 s). In the example shown here, H, ^{3}He, and ^{4}He are read out every spin, and heavier species are read out every two spins.

The matrix rate boxes are defined with up-loadable tables, and thus can be reconfigured during the mission. Because the trimming and offsets for each of the 4 small solid-state detectors and 3 large solid-state detectors may differ from each other, the box definitions (in analyzer channel numbers) are given separately for each detector. This makes it possible also to recover from any changes in detector response during the mission. The matrix box definitions also include priority assignments for use in the algorithm that allocates telemetry to PHA events.

3.5. Resource summary

Overall resources used by ULEIS are summarized in Table IX.

4. Performance

4.1. Geometry factor – time-of-flight path length

Table X summarizes the geometry factors for ULEIS, taking account of the transmissions of all high voltage harps and foil meshes, as well as the closable iris settings. Detector areas for the 7 solid-state detector elements are in Table VI. The flight paths for particles entering the telescope parallel to the axis are:

– START-1 foil to STOP foil: 50.0 ± 0.1 cm.

– START-2 foil to STOP foil: 32.6 ± 0.1 cm.

The uncertainties in the path length are due to the compliant mounting of the foil substrates (see Section 3.2.3).

TABLE IX
ULEIS resources

Mass[a,b]		
telescope and sunshade	11.5 kg	
analog electronics box	4.0	
data processing unit box	1.9	
interbox harnesses	1.0	
Total mass	18.4 kg	
Power	Nominal	Peak
telescope	2.2W	2.3
analog electronics box	10.1	10.9
DPU	2.5	3.4
operational heater	2.6	2.6
survival heater		4.6[c]
iris motor	0.0	2.0
Total power	17.4 W	21.2 W
Data rate	1000 bps	

[a]Telescope mounting bracket (2.7 kg) not included in mass.
[b]Thermal blankets not included.
[c]Survival heater is not included in peak power total since is it not operated when the instrument is powered.

4.2. TIMING ACCURACY

One key contribution to the isotopic resolution of ULEIS is the time-of-flight system. ULEIS uses a constant-fraction discrimination design supplied by Siegmund Scientific, Berkeley, CA, in order to achieve a timing dispersion of $<$300 ps FWHM. The constant-fraction discrimination minimizes the effects of time-of-flight walk, wherein start and stop timing signals of different amplitude produce amplitude-dependent times-of-flight. Walk is the major potential source of dispersion in the time-of-flight measurement, since the statistical nature of the secondary electron amplification in the MCPs produces broad ranges of START-1, START-2, and STOP timing signals, even for identical secondary electron yields from each of the foils. Section 4.3.1.2 discusses examples of the ULEIS time-of-flight system response with accelerator measurements.

TABLE X
ULEIS geometry factors

Detector	Individual geometry factor (cm^2 sr)			
Iris setting:	100%	25%	6%	1%
D1	0.078	0.019	0.0058	0.0010
D2	0.079	0.019	0.0058	0.0010
D3	0.079	0.019	0.0059	0.0010
D4	0.079	0.019	0.0059	0.0010
D5	0.318	0.077	0.0236	0.0040
D6	0.318	0.077	0.0236	0.0040
D7	0.318	0.077	0.0236	0.0040
Small SSD total	0.314	0.076	0.0234	0.0040
Large SSD total	0.954	0.231	0.0709	0.0121
Total	1.268	0.307	0.0942	0.0161

Note: Figures include loss of sensitivity due to transmission of harps and foil meshes (see Table III).

4.3. MASS RESOLUTION: ENERGY AND MASS DEPENDENCIES

The mass resolution of ULEIS is dependent on particle species and energy. Using Equation (1) to obtain the mass of an ion, we can determine the uncertainty in the measurement of its mass by

$$\left(\frac{\sigma_m}{m}\right)^2 = \left(\frac{\sigma_E}{E}\right)^2 + \left(\frac{2\sigma_\tau}{\tau}\right)^2 + \left(\frac{2\sigma_L}{L}\right)^2 , \tag{4}$$

where the terms on the right hand side of Equation (4) are the contributions from the uncertainties in the measured energy, time-of-flight, and path length, respectively. Figure 13 shows the dependence of each term on the right hand side of Equation (4) on the particle's incident energy using a calculation of the energy losses in the 3 ULEIS foils and nominal dispersions of the energy, time-of-flight, and position systems, and assuming $m = 16$ (Oxygen). At the instrument threshold near $\sim$45 keV $nucl^{-1}$, the uncertainty in the energy measurement dominates the mass dispersion since the noise in the energy system is a considerable fraction of the deposited energy (Ipavich et al., 1978; Zabel et al., 1980; Galvin, 1982). As the energy of the ions increases, the energy dispersion of the solid-state detectors remains about the same, and so the σ_E/E ratio and σ_m/m ratio decrease as shown in the figure. In contrast, the timing dispersion term $2\sigma_\tau/\tau$ increases with energy, since the time-of-flight becomes smaller. The energy and timing contributions to the dispersion σ_m becomes comparable near 0.6 MeV $nucl^{-1}$. As the ion energy

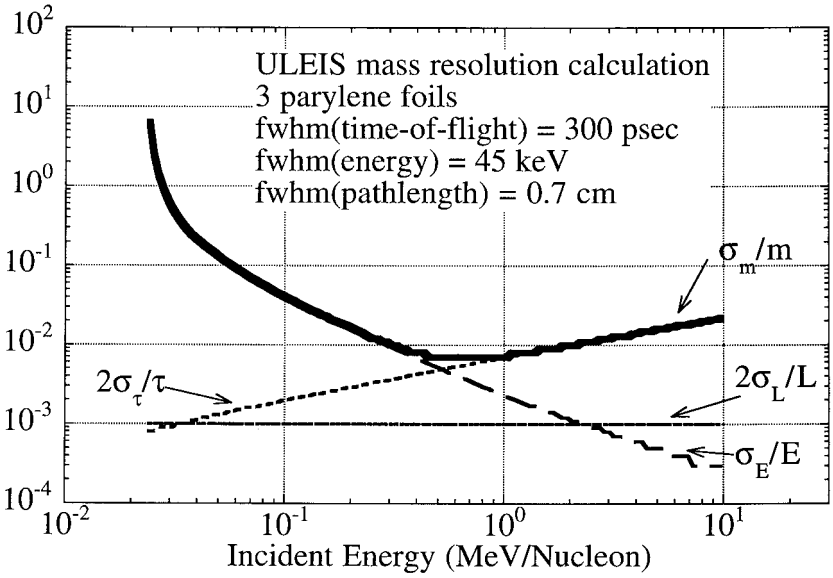

Figure 13. Calculated relative dispersions for ^{16}O in position, energy, and time-of-flight measurements for ULEIS versus incident particle energy.

increases further, the timing dispersion term continues to rise (dominating the mass dispersion) since for faster particles the measured time-of-flight τ is smaller. The path length dispersion term σ_L/L is much smaller than the other two (see Section 4.3.1.1). Thus, the three terms in Equation (4) combine to yield the σ_m/m curve with a characteristic minimum somewhat below 1 MeV nucl^{-1}. Examples of these dispersions using accelerator data are discussed below in Section 4.3.1.

The energy dependence of the energy and time-of-flight dispersions yields a minimum in the mass resolution near 1 MeV nucl^{-1} (see Figure 13). A given mass resolution therefore applies over a finite energy range. Table II lists sample energy ranges and reflects the dependence of σ_m on particle mass.

4.3.1. *Instrument Resolution: Examples*

We have measured the response of ULEIS to heavy ions at Brookhaven National Laboratory's Tandem van de Graaff and Lawrence Berkeley Laboratory's 88-inch cyclotron. Routine tests of ULEIS in vacuum with a ~1 MeV nucl^{-1} ^{4}He source verify the instrument's basic functions, but the larger amplitude timing signals from heavy ions at large accelerators are a more sensitive measure of the instrument's mass resolution.

4.3.1.1. *Position system.* Figure 14 shows the measured size of a 2 mm diameter beam of 1.85 MeV nucl^{-1} ^{40}Ar at the START-1, START-2, and STOP foils. The x-direction is along the 10-cm dimension of the MCPs. The particle beam was at normal incidence to the foils and collimated with a 2 mm diameter aperture

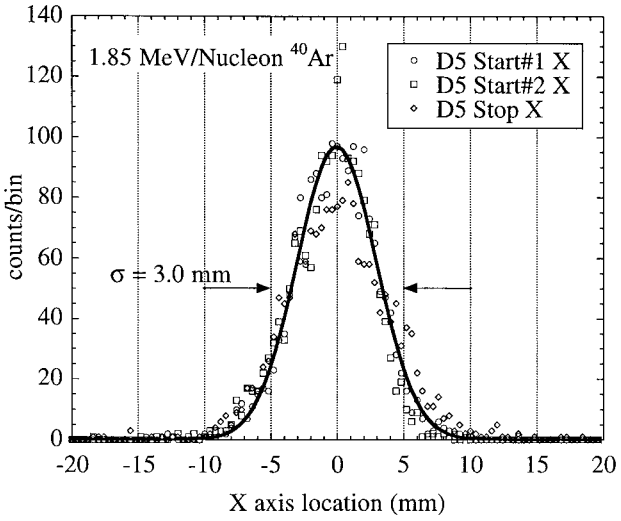

Figure 14. Position resolution for a normal incidence beam of 1.85 MeV nucl^{-1} ^{40}Ar measured at the 3 ULEIS foils.

upstream of ULEIS. The three position measurements have standard deviations of ∼3 mm, due to the cosine distribution of the secondary electrons emitted from the foils (Meckbach, 1976). Figure 14 also shows that, for this beam, there is little coulomb scattering in the ULEIS foils, since the beam diameter is virtually unchanged for the three foils. Propagated through the instrument from START-1 to STOP, an uncertainty of 3 mm in the calculated positions yields a typical uncertainty in the path length of $\sigma_L/L \sim 0.0006$. As shown in Figure 13, this is much less than other sources of dispersion in the instrument discussed below.

4.3.1.2. *Time-of-flight system.* Figure 15 is a histogram of the measured times-of-flight of 1.84 MeV nucl^{-1} ^{15}N measured between START-1 and STOP. The standard deviation is $\sigma_\tau = 114$ ps, ∼12% better than the design goal of 130 ps. Ions at this energy have small losses and straggling in the 3 foils compared to the total ion energy, so the measured 114 ps uncertainty is a result of the dispersions in the mirror and wedge assemblies and any residual walk in the time-of-flight electronics. Measured with ULEIS, heavy nuclei near 1 MeV nucl^{-1} typically have $\sigma_\tau < 130$ ps. The time-of-flight for 1.84 MeV nucl^{-1} ^{15}N is 26.6 ns between START-1 and STOP, so that $\sigma_\tau/\tau = 0.0045$.

The overall timing goal of <130 ps is very challenging, and requires excellent stability from the electronics and the MCP assemblies themselves. Since ULEIS particle measurements involve, e.g., interplanetary shocks or solar particle events that last only a few days, small drifts in the system over very long periods do not cause a problem with isotope identification during an event. Since ACE is spinning, and the instrument deck is continuously in sunlight, temperature variations

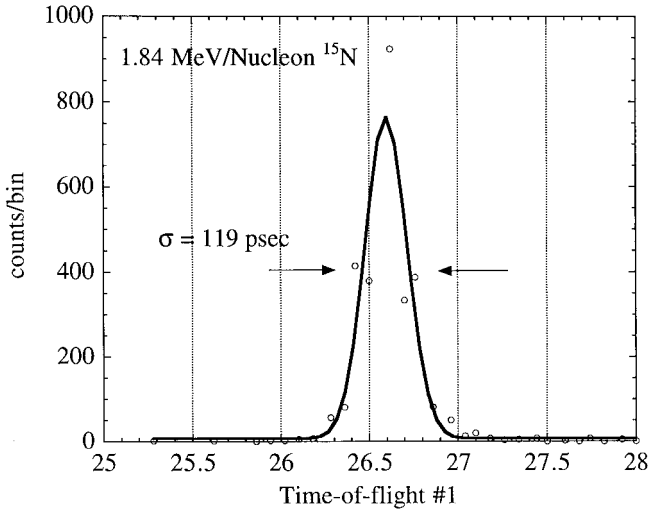

Figure 15. Time-of-flight distribution for mono-energetic ^{15}N measured between the START-1 and STOP foils.

over periods of a week should be very small. The most critical aspect of meeting the timing accuracy is due to the nonuniform response of the MCP stacks (see Section 3.2.4). Since the instrument pre-launch calibration only covered a few ion species and energies such as shown in Figure 15, it remains to be seen whether this timing resolution will be achieved over the entire sensitive area of the solid-state detectors and over the whole range of species and energies. If the timing dispersion is >130 ps, the mass resolution degrades incrementally, with the effect being most important at the high energy end of the instrument response window (see Figure 13 and Table II) and for higher mass isotopes.

4.3.1.3. *Energy system.* To determine if the ULEIS solid-state detector system is adequate for the mass resolution shown in Figure 13, we can compute the standard deviation of the energy measurements of the solid-state detector system for various 1–2 MeV nucl^{-1} heavy ion beams. The measured widths include effects of detector resolution and electronics noise; losses and straggling in the foils and pulse-height defect are small at these energies. For example, 2 MeV nucl^{-1} ^{16}O deposits 32.0 MeV in the solid-state detector with a σ_E of 0.160 MeV. Thus, $\sigma_E/E = 0.005$ and if all the uncertainty in mass was due to the energy system dispersion, then $\sigma_m/m = 0.005$ and $\sigma_m = 0.08$ amu at mass 16. This is a factor of 2 less than the $\sigma_m = 0.16$ amu design goal at mass 16.

4.3.1.4. *Mass resolution.* Figure 16 shows the mass resolution of ULEIS for several monoenergetic species near 1 MeV nucl^{-1}; masses were calculated directly from Equation (1). In applying Equation (1) we neglected the path length dispersion since the beam was parallel to the telescope axis and scattering is minimal

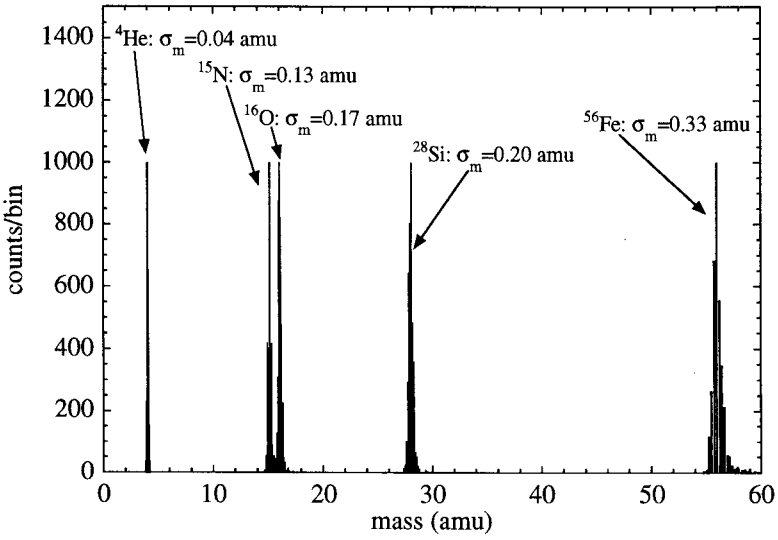

Figure 16. ULEIS mass distributions for ^{4}He and several heavy ion beams. Incident particle energies are all between 1 and 2 MeV nucl^{-1}.

at these energies. The mass histograms in Figure 16 also include the effects of dispersion in the energy system since they include all the measured energies for a given incident beam. Figure 17 compares the standard deviations of these mass distributions with the calculated response of ULEIS. In each case, the measured resolution is within ∼20% of that expected from Equation (4). Although there is only one calibration point per species shown in Figure 17 they are close to the energies where the instrument's mass dispersion is at its minimum value, and is dominated by the timing resolution.

4.4. BACKGROUND REJECTION

ULEIS has a naturally low background due to the coincidence requirements between (1) a start and a stop timing signal, producing a valid stop, and (2) between a valid stop and the trigger of a solid-state detector. ULEIS employs two times-of-flight, START-1 to STOP (TOF-1) and START-2 to STOP (TOF-2) in order to further reduce the contribution of possible background sources such as time-of-flight ringing and accidental coincidences. The two times-of-flight allow the rejection of events in the ground-based processing that do not have consistent times-of-flight.

Figure 18(a) shows the TOF-1/TOF-2 ratio as a function of TOF-1 for 1.84 MeV nucl^{-1} ^{15}N. Each point is an individual ion that triggered both times-of-flight systems and a solid-state detector; the solid horizontal lines show ±5% limits on the ratio of times-of-flight calculated from the distances between the foils. Figure 18(b) shows the effect of the time-of-flight constraint on the TOF-1 distribution. The bulk

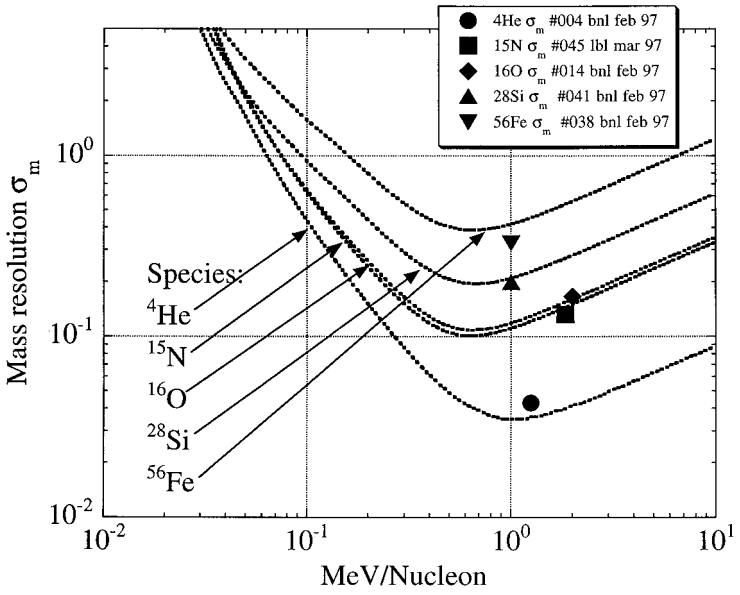

Figure 17. Comparison of measurements of the ULEIS mass resolution with calculations based on Equation (4).

of the events satisfy the constraint, while single-event outliers do not; these outliers would subsequently be rejected in the ground-based analysis. The two-parameter measurement is important in studies of rare isotopes such as ^{18}O whose abundance is only ∼0.2% of its neighbor ^{16}O.

In Figure 18(a) the points outside the valid limits form a 'Y' shaped pattern. The three branches of the 'Y' correspond to three different types of events. First, the upper right branch of the 'Y' is due to events whose TOF-1 is about 4 nanoseconds too long; the relatively long time offset, and the clustering of points around a single value indicates that these events are associated with ringing somewhere in the electronics that causes a time-of-flight that is too long. The vertical branch of the 'Y' is caused by the same effect except for the TOF-2 signal: this makes the TOF-1/TOF-2 ratio too small, and is uncorrelated with the TOF-1 value as seen. Thirdly, there is the upper left branch of the 'Y', which has values of TOF-1 that are too low, and these occur in correlation with values of TOF-2 that are too low, but that are not in the expected ratio of TOF-1/TOF-2. The mechanisms leading to these types of background events are not understood. Note that the background events in Figure 18(a) are less than 1% of the main peak (see Figure 18(b)).

4.5. EFFICIENCY

Secondary electron yields for ions passing through thin foils roughly follow the $\mathrm{d}E/\mathrm{d}x$ of the particles, and are therefore both species and energy dependent. For H and He, the forward secondary electron yield (appropriate for the two START

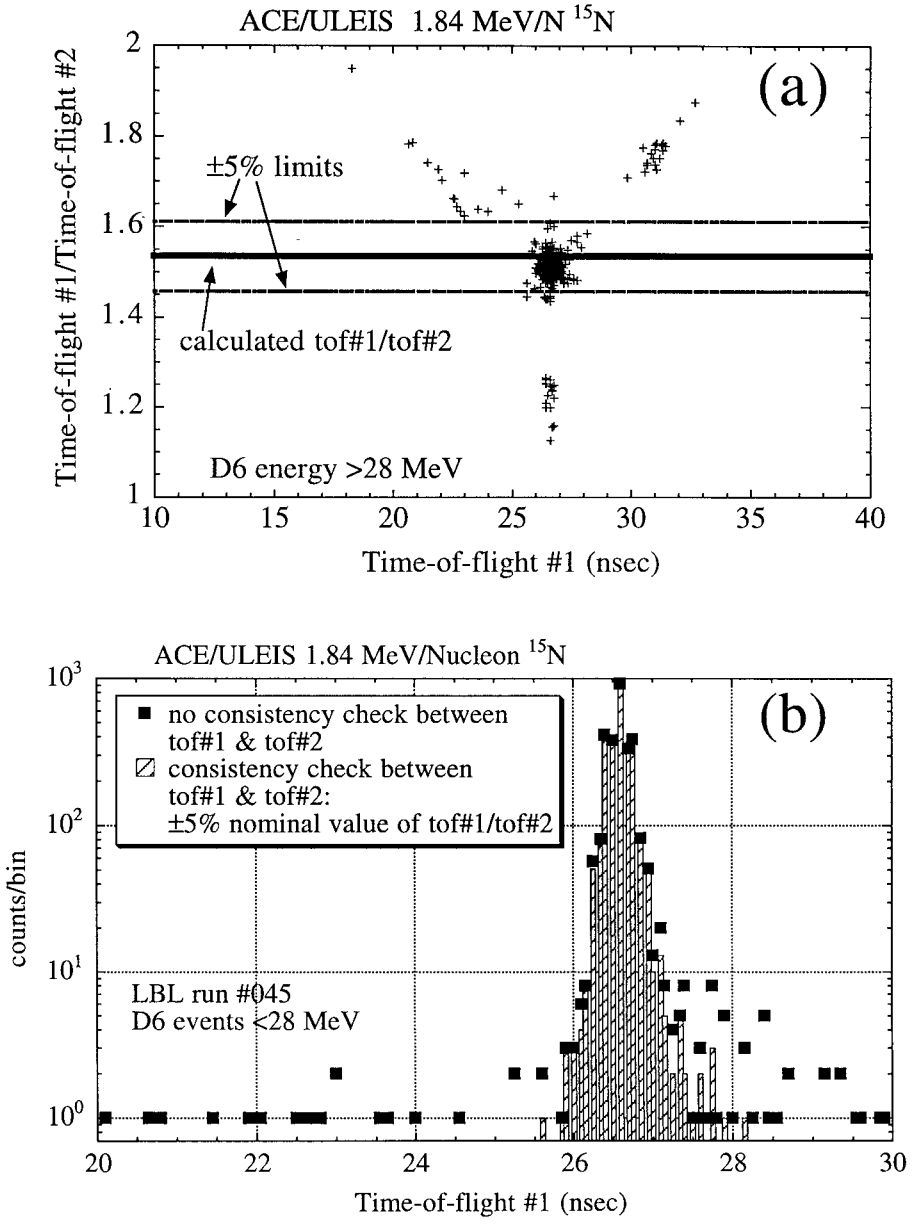

Figure 18. (a) Comparison of expected ratio of times-of-flight with measurements of 1.84 MeV nucl^{-1} ^{15}N. Most events satisfy the ±5% constraint on TOF-1/TOF-2. (b) Effect of time-of-flight consistency check on the measured TOF-1 distribution.

TABLE XI
Triggering efficiencies for EPACT/STEP telescope (estimated) at 500 keV nucl^{-1}

Element	Efficiency
H	0.03
He	0.22
C	0.97
O	1.00
Fe	1.00

foils) peaks at roughly 3–10 electrons around a few hundred keV nucl^{-1}, while the backward emission (appropriate for the STOP foil) is a factor of 2 lower (Clerc et al., 1973; Meckbach, 1976; Pferdekämper and Clerc, 1977). An additional important effect is the dead area of the MCP front surfaces, which is approximately 50%. The triggering efficiency of the plates for single electrons hitting a channel may also be less than unity since the plate operating bias is usually selected to minimize ion feedback. Since both a start and a stop MCP trigger are required to analyze an event, the overall telescope efficiency is proportional to the square of the efficiency for a single MCP stack trigger. These effects combine to produce overall triggering efficiencies that are much less than unity for H and He, while for heavier ions the efficiency is close to 1. At the current writing, these efficiencies have not been fully determined for the ULEIS telescope, but as a guide, Table XI lists 0.5 MeV nucl^{-1} efficiencies for the EPACT/STEP telescope on the WIND spacecraft (von Rosenvinge et al., 1995), which covers a similar energy range to ULEIS. Because of the dependence on $\mathrm{d}E/\mathrm{d}x$ which peaks in the range 0.1–1 MeV nucl^{-1}, the efficiencies are lower outside that energy range.

5. Flight Operations

ULEIS operates in its normal mode continuously except for about one hour/month when an on-board calibrator is activated by ground command. Dual small calibration alpha-particle sources are mounted inside the iris cover for testing instrument particle response in flight.

The multiparameter measurements returned by ULEIS for each ion allow for self-calibration of the instrument in space. Any shifts in detector response will result in a shift of particle tracks in the time-vs-energy data, that can be easily detected and corrected for. If necessary, there is a provision for uploading new look-up tables for the matrix rates to take account of possible drifts. The ability to

adjust detector and MCP bias and multiple redundancy in the solid-state detector array helps protect against a wide range of possible drifts and malfunctions.

Acknowledgements

We would like to thank the many dedicated individuals in the Space Physics Group of the Department of Physics at the University of Maryland, and in the Space Department of the Johns Hopkins University Applied Physics Laboratory for the design, construction, checkout, calibration, and flight qualification of the ULEIS instrument. We thank the staffs of the Brookhaven National Laboratory tandem Van de Graaff, and the Lawrence Berkeley Laboratory 88-inch cyclotron, including the Aerospace Corporation Space Sciences Department, for their support in accelerator runs for the development and calibration of the ULEIS instrument. Finally, we thank the ACE project office at the Goddard Space Flight Center, and the ACE Payload Management Office at Caltech for their enthusiastic and continuing support of the ULEIS effort. This work was supported in part by NASA under cooperative agreement PC 38597 with the California Institute of Technology.

References

Ajello, J. M.: 1990, 'Solar Minimum Lα Background Observations from Pioneer Venus Orbiter Ultraviolet Spectrometer: Solar Wind Latitude Variation', *J. Geophys. Res.* **95**(A9), 14855

Anders, E. and Ebihara, M.: 1982, 'Solar-System Abundances of the Elements', *Geochim. Cosmochim. Acta*. **46**, 2363.

Anger, H. O.: 1966, *Trans. Instr. Soc. Am.* **5**, 311.

Barnes, C. W. and Simpson, J. A.: 1976, 'Evidence for Interplanetary Acceleration of Nucleons in Corotating Interaction Regions', *Astrophys. J.* **210**, L91.

Breneman, H. H. and Stone, E. C.: 1985, 'Solar Coronal and Photospheric Abundances from Solar Energetic Particle Measurements', *Astrophys. J.* **299**, L57.

Chiu, M. C., et al.: 1998, 'ACE Spacecraft', *Space Sci. Rev.* **86**, 257.

Clerc, H.-G., Gehrhardt, H. J., Richter, L., and Schmidt, K. H.: 1973, 'Heavy-Ion Induced Secondary Electron Emission – a Possible Method for Z-Identification', *Nucl. Instr. Methods* **113**, 325.

Coplan, M. A., Ogilvie, K. W., Bochsler, P., and Geiss, J.: 1990, 'Space-Based Measurements of Elemental Abundances and Their Relation to Solar Abundances', *Solar Phys.* **128**, 195.

Cummings, A. C. and Stone, E. C.: 1996, 'Composition of Anomalous Cosmic Rays and Implications for the Heliosphere', *Adv. Space Res.* **78**, 117.

Fisk, L. A.: 1978, '^{3}He-Rich Flares: a Possible Explanation', *Astrophys. J.* **224**, 1048.

Fisk, L. A., Kozlovsky, B., and Ramaty, R.: 1974, 'An Interpretation of the Observed Oxygen and Nitrogen Enhancements in Low-Energy Cosmic Rays', *Astrophys. J.* **190**, L35.

Fisk, L. A. and Lee, M. A.: 1980, 'Shock Acceleration of Energetic Particles in Corotating Interaction Regions in the Solar Wind', *Astrophys. J.* **237**, 620.

Fisk, L. A., Schwadron, N. A., and Zurbuchen, T. H.: 1998, 'On the Slow Solar Wind', *Space Sci. Rev.* **86**, 51.

Galvin, A. B.: 1982, '*Charge States of Heavy Ions in the Energy Range ∼30–130 keV/Q Observed in Upstream Events Associated with the Earth's Bow Shock*', Dept. of Physics, University of Maryland.

Galvin, A. B., Ipavich, F. M., Cohen, C. M. S., Gloeckler, G., and von Steiger, R.: 1995, 'Solar Wind Charge States Measured by Ulysses/SWICS in the Solar Polar Hole', *Space Sci. Rev.* **72**, 65.

Galvin, A. B., Ipavich, F. M., Gloeckler, G., Hovestadt, D., Klecker, B., and Scholer, M.: 1984, 'Solar Wind Ionization Temperatures Inferred from the Charge State Composition of Diffuse Events', *J. Geophys. Res.* **89**, 2655.

Gloeckler, G., Bedini, P., Bochsler, P., Fisk, L. A., Geiss, J., Ipavich, F. M., Cani, J., Fischer, J., Kallenbach, R., Miller, J., Tums, E. V., and Wimmer, R.: 1998 'Investigation of the Composition of Solar and Interstellar Matter Using Solar Wind and Pickup Ion Measurements with SWICS and SWIMS on the ACE Spacecraft', *Space Sci. Rev.* **86**, 497.

Gloeckler, G., Geiss, J., Roelof, E. C., Fisk, L. A., Ipavich, F. M., Ogilvie, K. W., Lanzerotti, L. J., von Steiger, R., and Wilken, B.: 1994, 'Acceleration of Interstellar Pickup Ions in the Disturbed Solar Wind Observed on Ulysses', *J. Geophys. Res.* **99**, 17637.

Gloeckler, G., Hovestadt, D., and Fisk, L. A.: 1979, 'Observed Distribution Functions of H, He, C, O, and Fe in Corotating Energetic Particle Streams: Implications for Interplanetary Acceleration and Propagation', *Astrophys. J.* **230**, L191.

Ipavich, F. M., Lundgren, R. A., Lambird, B. A., and Gloeckler, G.: 1978, 'Measurement of Pulse-Height Defect in Au-Si Detector for H, He, C, N, O, Ne, Ar, Kr from $\sim$2 to $\sim$400 keV nucl^{-1}', *Nuc. Instr. Methods* **154**, 291.

Jokipii, J. R.: 1996, 'Theory of Multiply-Charged Anomalous Cosmic Rays', *Astrophys. J.* **466**, 47.

Klecker, B.: 1995, 'The Anomalous Component of Cosmic Rays in the 3-D Heliosphere', *Space Sci. Rev.* **72**, 419.

Klecker, B., Oetliker, M., Blake, J. B., Hovestadt, D., Mason, G. M., Mazur, J. E., and McNab, M. C.: 1997, 'Multiply Charged Anomalous Cosmic Ray N, O, and Ne: Observations with HILT/SAMPEX', *Proc. 25th Int. Cosmic Ray Conf., Durban* **1**, 273.

Lapington, J. S. and Schwarz, H. E.: 1986, 'The Design and Manufacture of Wedge and Strip Anodes', *IEEE Trans. Nucl. Sci.* **NS-33**, 288.

Luhn, A., Klecker, B., Hovestadt, D., and Möbius, E.: 1985, 'The Mean Ionic Charge State of Silicon in ^{3}He-Rich Solar Flares', *Proc. 19th Int. Cosmic Ray Conf., La Jolla* **4**, 285.

Mason, G. M., Gloeckler, G., and Hovestadt, D.: 1984, 'Temporal Variations of Nucleonic Abundances in Solar Flare Energetic Particle Events. II. Evidence for Large Scale Shock Acceleration', *Astrophys. J.* **280**, 902.

Mason, G. M., Mazur, J. E., Dwyer, J. R., Reames, D. V., and von Rosenvinge, T. T.: 1997, 'New Spectral and Abundance Features of Interplanetary Heavy Ions in Corotating Interaction Regions', *Astrophys. J.* **486**, L149.

Mason, G. M., Mazur, J. E., and Hamilton, D. C.: 1994, 'Heavy Ion Isotopic Anomalies in ^{3}He-Rich Solar Particle Events', *Astrophys. J.* **425**, 843.

Mazur, J. E., Mason, G. M., Klecker, B., and McGuire, R. E.: 1992, 'The Energy Spectra of Solar Flare Hydrogen, Helium, Oxygen, and Iron: Evidence for Stochastic Acceleration', *Astrophys. J.* **401**, 398.

Mazur, J. E., Mason, G. M., Klecker, B., and McGuire, R. E.: 1993, 'The Abundances of Hydrogen, Helium, Oxygen, and Iron Accelerated in Large Solar Particle Events', *Astrophys. J.* **404**, 810.

McComas, D. J., Bame, S. J., Barker, P., Feldman, W. C., Phillips, J. L., Riley, P., and Griffee, J. W.: 1998, 'Solar Wind Electron Proton Alpha Monitor (SWEPAM) for the Advanced Composition Explorer', *Space Sci. Rev.* **86**, 563.

McDonald, F. B., Teegarden, B. J., Trainor, J. H., von Rosenvinge, T. T., and Webber, W. R.: 1976, 'The Interplanetary Acceleration of Energetic Nucleons', 1976, *Astrophys. J.* **203**, L149.

Meckbach, W.: 1976, 'Secondary Electron Emission from Foils Traversed by Ion Beams', in I. A. Sellin and D. J. Pegg (eds.), *Beam-Foil Spectroscopy*, Plenum Press, New York, p. 577.

Mewaldt, R. A., Selesnick, R. S., Cummings, J. R., Stone, E. C., and von Rosenvinge, T. T.: 1996, 'Evidence for Multiply Charged Anomalous Cosmic Rays', *Astrophys. J.* **466**, L43.

Mewaldt, R. A. and Stone, E. C.: 1989, 'Isotope Abundances of Solar Coronal Material Derived from Solar Energetic Particle Measurements', *Astrophys. J.* **337**, 959.

Mewaldt, R. A., Stone, E. C., Vidor, B., and Vogt, R. E.: 1976, 'Isotopic and Elemental Composition of the Anomalous Low-Energy Cosmic Ray Fluxes', *Astrophys. J.* **205**, 931.

Mewaldt, R. A., Stone, E. C., and Vogt, R. E.: 1978, 'The Radial Diffusion Coefficient of 1.3–2.3 MeV Protons in Recurrent Proton Streams', *Geophys. Res. Letters* **5**, 965.

Miller, J. A.: 1998, 'Particle Acceleration in Impulsive Solar Flares', *Space Sci. Rev.* **86**, 79.

Miller, J. A. and Reames, D. V.: 1995, 'Heavy Ion Acceleration by Cascading Alfvén Waves in Impulsive Solar Flares', *High Energy Solar Physics*, AIP Conf. Proc. 374, Am. Inst. Physics, New York, p. 450.

Möbius, E., et al.: 1998, 'The Solar Energetic Particle Ionic Charge Analyzer (SEPICA) and the Data Processing Unit (S3DPU) for SWICS, SWIMS, and SEPICA', *Space Sci. Rev* **86**, 449.

Möbius, E., Scholer, M., Hovestadt, D., Klecker, B., and Gloeckler, G.: 1982, 'Comparison of Helium and Heavy Ion Spectra in ^{3}He-Rich Solar Flares with Model Calculations Based on Stochastic Fermi Acceleration in Alfvén Turbulence', *Astrophys. J.* **259**, 397.

Pesses, M. E., Jokipii, J. R., and Eichler, D.: 1981, 'Cosmic Ray Drift, Shock Wave Acceleration, and the Anomalous Component of Cosmic Rays', *Astrophys. J.* **246**, L85.

Pferdekämper, K. E. and Clerc, H.-G.: 1977, 'Energy Spectra of Secondary Electrons Ejected by Ions from Foils', *Zeitschrift Physik A* **280** 155.

Powell, F. R., Keski-Kuha, R. A. M., Zombeck, M. V., Goddard, R. E., Chartas, G., Townsley, L. K., Möbius, E., Davis, J. M., and Mason, G. M.: 1997, 'Metalized Polyimide Filters for X-ray Astronomy and Other Applications', Invited Review Paper, *Proc. SPIE (The International Society for Optical Engineering)*.

Ramaty, R., Mandzhavidze, N., and Kozlovsky, B.: 1995, 'Solar Atmospheric Abundances from Gamma Ray Spectroscopy', *High Energy Solar Physics* p. 172.

Reames, D. V., Barbier, L. M., and Ng, C. K.: 1996, 'The Spatial Distribution of Particles Accelerated by Coronal Mass Ejection-Driven Shocks', *Astrophys. J.* **466**, 473.

Reames, D. V., Barbier, L. M., von Rosenvinge, T. T., Mason, G. M., Mazur, J. E., and Dwyer, J. R.: 1997, 'Energy Spectra of Ions Accelerated in Impulsive and Gradual Solar Events', *Astrophys. J.* **483**, 515.

Reames, D. V., von Rosenvinge, T. T., and Lin, R. P.: 1985, 'Solar ^{3}He-Rich Events and Nonrelativistic Electron Events: a New Association', *Astrophys. J.* **292**, 716.

Richardson, I. G. and Hynds, R. J.: 1990, 'Spectra of $>$35 keV ions in Corotating Ion Enhancements at 1 AU', *Proc. 21st Int. Cosmic Ray Conf., Dublin* **5**, 337.

Selesnick, R. S., Cummings, A. C., Cummings, J. R., Leske, R. A., Mewaldt, R. A., Stone, E. C., and von Rosenvinge, T. T.: 1993, 'Coronal Abundances of Neon and Magnesium Isotopes from Solar Energetic Particles', *Astrophys. J.* **418**, L45.

Siegmund, O. H. W., Lampton, M., Bixler, J., Bowyer, S., and Malina, R. F.: 1986a, 'Operation Characteristics of Wedge and Strip Readout Systems', *IEEE Trans. Nucl. Sci.* **33**(1), 724.

Siegmund, O. H. W., Lampton, M., Bixler, J., Chakrabarti, S., Vallerga, J., Bowyer, S., and Malina, R. F.: 1986b, *J. Opt. Soc. Amer. A* **3**, 2139.

Starzecki, W., Stefanini, A. M., Lunardi, S., and Signorini, C.: 1982, 'A Compact Time-Zero Detector for Mass Identification of Heavy Ions', *Nucl. Instr. Method.* **193**, 499.

Stone, E. C., et al.: 1989, '*Phase A Study of an Advanced Composition Explorer'*, California Institute of Technology.

Stone, E. C., et al.: 1998a, 'The Cosmic Ray Isotope Spectrometer for the Advanced Composition Explorer', *Space Sci. Rev.* **86**, 285.

Stone, E. C., et al.: 1998b, 'The Solar Isotope Spectrometer for the Advanced Composition Explorer', *Space Sci. Rev.* **86**, 355.

von Rosenvinge, T. T., et al.: 1995, 'The Energetic Particles: Acceleration, Composition, and Transport (EPACT) Investigation on the Wind Spacecraft', *Space. Sci. Rev.* **71**, 155.

von Steiger, R. and Geiss, J.: 1989, 'Supply of Fractionated Gases to the Corona', *Astron. Astrophys.* **225**, 222.
Zabel, T. H., Fewell, M. P., Kean, D. C., and Spear, R. H.: 1980, 'The Response of Silicon Surface-Barrier Detectors to Light and Heavy Ions', *Nucl. Instr. Methods* **174**, 459.